energies

MDPI

Article

A Low-Voltage Mitigation Method for Rural Distribution Transformer Areas Based on Power-Mileage Aggregation

Donglai Tang [1,*], Peng Zhou [1,*], Degang Gan [1], Youbo Liu [2], Xu Zhong [1] and Li Tang [1]

[1] Sichuan SGIT Technology Co., Ltd., Chengdu 610094, China; smallboxstar@163.com (D.G.); jinzhongjiuri@163.com (X.Z.); tangliyeah@163.com (L.T.)
[2] School of Electrical Engineering, Sichuan University, Chengdu 610207, China; liuyoubo@scu.edu.cn
* Correspondence: tangdonglai@sohu.com (D.T.); 19950231220@163.com (P.Z.); Tel.: +86-139-8185-2422 (D.T.)

Abstract

Low-voltage violations in rural distribution transformer areas (RDTAs) are a persistent and widespread problem in China, affecting over 5% of such areas and compromising the power supply quality for millions of rural end-users. These violations are primarily caused by long supply distances, undersized conductors, dispersed load distributions, and low power factors at terminal feeders, resulting in degraded equipment performance, increased line losses, and hindered integration of renewable distributed generation. The key to mitigating such violations lies in the rapid and coordinated regulation of primary equipment. Considering the actual equipment configurations in rural distribution transformer areas, a low-voltage mitigation method based on power-mileage aggregation is proposed. First, a generative adversarial network is employed to preprocess the collected electrical data, and device ranging is achieved through power-line characteristic pulses, enabling the spatiotemporal distribution analysis of low-voltage phenomena. Second, based on the line lengths from power sources—including distributed generators, soft open points, energy storage systems, and distribution transformers—to the smart meters, a power-mileage aggregation metric is developed to quantify the impact of power-source output variations on low-voltage meters. Subsequently, with the objective of minimizing the power mileage for low-voltage mitigation, the Newton iteration method is applied to determine the optimal output powers of energy storage systems and soft open points. The effectiveness of the proposed method is validated through case studies. Comparative analyses with optimal power flow, second-order cone programming, and interval robust control demonstrate that the proposed approach achieves superior low-voltage mitigation performance while maintaining higher economic efficiency.

Keywords: rural distribution transformer area; low-voltage mitigation; energy storage system; soft open point; generative adversarial network; Newton iteration method

Check for updates

Academic Editor: José Antonio Domínguez-Navarro

Received: 3 July 2026
Revised: 27 July 2026
Accepted: 1 August 2026
Published: 4 August 2026

Copyright: © 2026 by the authors. Licensee MDPI, Basel, Switzerland. This article is an open access article distributed under the terms and conditions of the Creative Commons Attribution (CC BY) license.

1. Introduction

Rural distribution transformer areas (RDTAs) serve as the fundamental infrastructure through which power supply companies deliver electricity services to rural end-users [1,2]. In China, RDTAs are geographically extensive—often with supply radii exceeding 1000 m—and equipped with outdated power facilities, including undersized conductors (typically 35–50 mm^2) and aging transformers. Despite multiple rounds of rural grid renovations, persistent challenges, such as long supply distances, undersized conductors, poor conductor operating conditions, dispersed load distributions, and low power factors (often below

0.85) at terminal users, have resulted in frequent low-voltage violations at feeder ends. According to statistics from the State Grid Corporation of China, RDTAs with low-voltage violations account for over 5% of the total in China, a figure significantly higher than the 1% observed in developed countries such as Germany and Japan [3]. Field measurements from typical RDTAs show that the minimum voltage at terminal consumer meters (CMs) can drop to 187.8 V during peak load periods, substantially below the 198 V lower limit prescribed by the Chinese Power Quality Standard.

The negative impacts of these low-voltage violations are substantial and multifaceted. First, end-users experience degraded power quality, which can cause malfunction or reduced efficiency of household appliances (e.g., refrigerators, air conditioners, and water pumps) and agricultural equipment (e.g., irrigation systems and grain dryers), directly affecting rural livelihoods and productivity. Second, low-voltage conditions increase line losses significantly: operating at 190 V instead of 220 V on a feeder with constant power loads results in approximately 15% higher current, leading to 30% higher I^2R losses along the distribution lines, which reduces overall energy efficiency and increases operational costs for grid companies. Third, the increased current stress accelerates the aging of transformers and conductors, reduces equipment lifespan, and increases maintenance frequency and replacement costs. Fourth, low-voltage constraints limit the hosting capacity for renewable distributed generation (DG), as photovoltaic (PV) systems cannot be fully utilized when grid voltage is already low, thereby hindering the rural photovoltaic poverty alleviation program initiated in 2016 [4]. While DGs contribute to node voltage elevation [4], the intermittency and stochastic nature of photovoltaic and wind power generation also induce voltage fluctuations, further compromising the effectiveness of low-voltage mitigation strategies [5,6]. Consequently, research on low-voltage mitigation in RDTAs is of paramount importance for improving rural power supply quality, enhancing energy efficiency, and enabling the integration of renewable energy resources.

In recent years, numerous studies have been conducted on voltage control in distribution networks. Conventional voltage regulation schemes employ on-load tap-changing transformers [7–9], shunt capacitors [10,11], and multipurpose grid-connected converters [12]. However, these devices are incapable of frequent regulation, making it difficult to meet the rapid response requirements under high DG penetration scenarios. DG inverters can also effectively regulate voltage. In the domain of reactive power control, a distributed voltage control method based on state–space linear transformation was proposed in [13], while a reactive power coordination strategy for distributed photovoltaics considering imperfect communication was presented in [14]. In terms of active power control, voltage regulation was achieved through DG active power curtailment in [15,16], and a cooperative control method was employed in [17] to balance the frequent switching of regulation devices and DG power output. Although DG inverters are effective for voltage regulation, most DGs in RDTAs are invested in and constructed by end-users, rendering them difficult for grid companies to directly control. As power electronic devices installed at tie switches, soft open points (SOPs) enable voltage control by adjusting power flows between low-voltage feeders [18,19]. Studies in [20,21] utilized SOPs to coordinate the switching of capacitor banks and the tap-changing of on-load tap-changing transformers to address voltage issues caused by high renewable DG penetration. However, due to the large number of widely distributed DGs and low communication reliability, these SOP-based schemes are difficult to implement effectively. Meanwhile, with the substantial reduction in energy storage costs, energy storage systems (ESSs) have become a key means of distribution network energy management, owing to their capability for optimal power flow distribution and efficient power regulation. A robust cooperative optimization control for ESS active and reactive power considering wind power uncertainty was proposed

in [22]; a two-stage coordinated control method utilizing conventional voltage regulation devices and distributed ESSs was presented in [23]. Nevertheless, the aforementioned methods generally adopt centralized or distributed control architectures, both of which rely on high-performance processors and advanced communication infrastructure, making them difficult to deploy in current RDTA environments. Moreover, these methods do not address the issue of missing data during data acquisition and transmission, nor its impact on voltage control performance.

In addition to the above methods, distribution network upgrades based on the root causes of low-voltage violations can enhance supply capacity and effectively resolve low-voltage issues. Specific measures include replacing distribution transformers and upgrading supply lines. The former addresses excessive voltage losses and insufficient transformer capacity in aging transformers [24], while the latter targets undersized conductors and excessive supply radii. However, terminal low-voltage issues in RDTAs are primarily caused by dispersed loads, long supply distances, and undersized conductors; thus, transformer replacement alone cannot fully resolve the problem. Although line upgrades can effectively mitigate low-voltage violations [25], such approaches involve long implementation cycles, high costs, and fail to fully utilize existing lines and equipment, limiting their significance for large-scale application [26].

Different than traditional voltage evaluation indicators that consider only power magnitude or line impedance separately, the concept of power-mileage aggregation is innovatively proposed. The concept couples power output with power delivery distance to enable unified quantification of the voltage regulation capability of ESSs and SOPs. This core idea fundamentally distinguishes itself from existing mainstream technical routes, namely, sensitivity-based linear voltage control and static distance-weighted regulation. Sensitivity-based methods establish fixed voltage–power sensitivity matrices via linear power flow approximation; however, they fail to dynamically couple the real-time power outputs of DGs, ESSs, and SOPs with feeder transmission distances, leading to prominent linearization errors under fluctuating photovoltaic generation. Static distance-weighted schemes merely adopt constant line lengths as weighting factors, thereby decoupling power magnitude from spatial information and failing to capture the superimposed voltage-lifting effects of multiple distributed resources. To overcome these two critical limitations, an innovative power-mileage aggregation metric is introduced that fuses instantaneous power outputs and high-precision physical feeder lengths into a unified spatiotemporal quantitative index, enabling a low-complexity Newton-based optimization that minimizes control effort under data-imperfect conditions without relying on full network topology, admittance parameters, or high-performance communication infrastructure. The overall workflow comprises three stages: low-voltage customer analysis, power-mileage aggregation, and voltage regulation. Specifically, electrical data are collected via time-synchronized intelligent fusion terminals (IFTs), preprocessed using a generative adversarial network (GAN), and supplemented with device ranging through power-line characteristic pulses to analyze the spatiotemporal distribution of low-voltage violations. Subsequently, a power-mileage aggregation model is established, followed by a voltage mitigation model incorporating ESSs and SOPs, which is solved using the Newton–Raphson (NR) algorithm. The effectiveness of the proposed method is validated through case studies, and comparative analyses with optimal power flow, second-order cone programming, and interval robust control, demonstrating that the proposed approach achieves superior low-voltage mitigation performance while significantly reducing mitigation costs. The proposed method thus offers a practically viable and cost-effective solution tailored to the unique constraints of rural distribution networks—a contribution that has not been previously reported in the existing literature.

2. RDTA Low-Voltage Mitigation Workflow

The proposed low-voltage mitigation method for RDTAs based on power-mileage aggregation comprises three sequential stages: low-voltage customer analysis, power-mileage aggregation analysis, and voltage regulation. The overall workflow is illustrated in Figure 1.

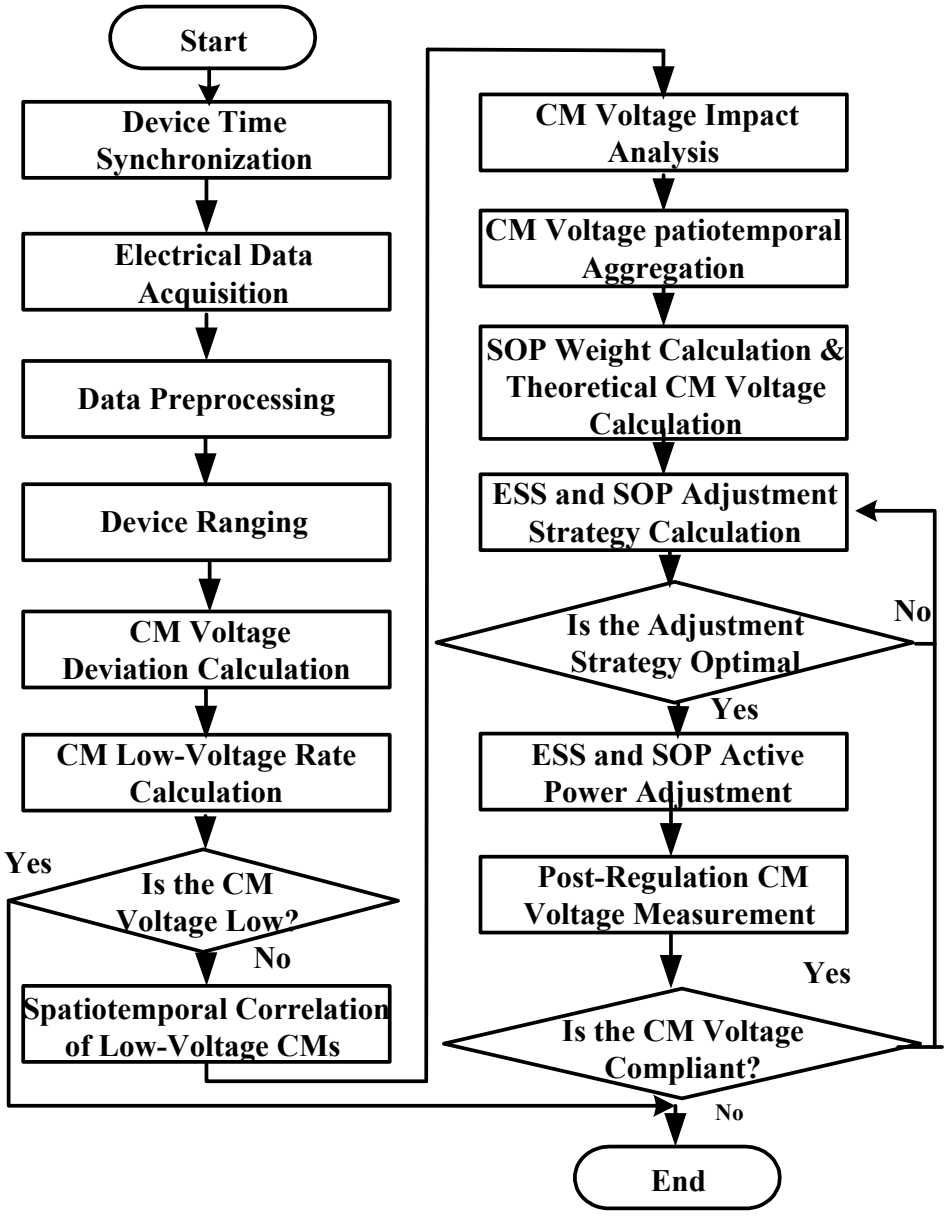


Figure 1. Low-voltage mitigation workflow in RDTAs.

(1) Low-Voltage Customer Analysis

The objective of low-voltage customer analysis is to acquire the spatiotemporal distribution characteristics of low-voltage CMs, thereby providing fundamental data for subsequent mitigation efforts. First, the IFT in the RDTAs receives time synchronization signals from the grid clock source [27] and distributes the timing signals to DGs, ESSs, SOPs, and CMs to ensure data acquisition consistency. Second, electrical parameters—including voltage, current, and power factor—are collected and preprocessed to eliminate the influence of anomalous data. Third, ranging measurements are performed for all power sources—including distribution transformers, DGs, ESSs, and SOPs—to provide

spatial data on line lengths. Finally, the low-voltage ratio of each CM is calculated and its spatiotemporal distribution characteristics are analyzed.

(2) Power-Mileage Aggregation Analysis

The purpose of power-mileage aggregation analysis is to establish the quantitative relationship between power-source output power, CM load variations, and CM voltage deviations, thereby providing foundational data for ESS and SOP power control. By considering power-source output, CM load variations, and the line lengths from power sources to CMs, the theoretical CM voltage variation is derived through power-mileage aggregation and the voltage control weights for ESSs and SOPs are subsequently calculated.

(3) Voltage Regulation

Voltage regulation aims to mitigate low-voltage violations at CMs. First, a control strategy is formulated based on the voltage control weights of ESSs and SOPs; iterative optimization is performed until the optimal regulation effect is achieved. Second, the active power outputs of ESSs and SOPs are adjusted according to the determined strategy. Finally, post-regulation CM voltages are measured and the strategy is dynamically adjusted until all CM voltages comply with the required standards.

3. RDTA Low-Voltage Regulation Model

3.1. Low-Voltage User Analysis

3.1.1. RDTA Time Synchronization and Data Acquisition

Since 2020, State Grid Corporation of China has been developing a new generation of smart electricity meters based on international recommendations for electricity meters. Through the Intelligent Fusion Terminal (IFT), functions, including high-precision device time synchronization, electrical data acquisition, distributed generation (DG) control, and high-speed power-line carrier communication, have been realized [28], providing a foundation for the large-scale application investigated in the present work.

Time synchronization is the process of distributing a reference time to other devices in the RDTA system [29]. First, after receiving the BeiDou-based reference master clock from the power grid, the IFT transmits a forward time-synchronization signal t^{N} with a reference timestamp to devices such as the CM, DG, and SOP. Subsequently, each device calculates the deviation between its current time *t*^D^ and the forward synchronization signal. Finally, each device sends a reverse time-synchronization signal t^{L} containing its current device time t^{D} back to the IFT, which then calculates the deviation from the reverse signal to obtain the synchronization error t^{F}:

$$t^{\mathrm{F}} = \frac{1}{m_{\mathrm{a}}} \sum_{k=1}^{m_{\mathrm{a}}} \frac{\left(t_k^{\mathrm{N}} - t_k^{\mathrm{D}}\right) + \left(t_k^{\mathrm{L}} - t_k^{\mathrm{D}}\right)}{2} \tag{1}$$

where m_{a} is the number of synchronization rounds issued by the IFT, equal to the number of devices; t_k^{N} is the forward synchronization signal time of the IFT in the k-th round; t_k^{L} is the reverse synchronization signal time of the device in the k-th round; and t_k^{D} is the current time of the device in the k-th round.

The device time t^{B} of the CM, DG, SOP, and other equipment is calculated as:

$$t^{\mathrm{B}} = t^{\mathrm{D}} + t^{\mathrm{F}} \tag{2}$$

The data acquisition frequency of RDTA devices is related to the granularity of low-voltage regulation: a higher acquisition frequency yields finer regulation granularity. The acquisition frequency is set to 15 min/interval. After time synchronization, the IFT collects voltage and power data from each device through scheduled acquisition tasks.

The data acquisition frequency of RDTA devices is related to the granularity of low-voltage regulation: a higher acquisition frequency yields finer regulation granularity. The acquisition frequency is set to 15 min/interval, which is consistent with the technical specifications of the State Grid Corporation for low-voltage distribution station area monitoring. This interval is widely adopted in practical RDTA systems, as it provides sufficient time resolution to capture daily load variations and low-voltage events while maintaining manageable data volumes for communication, storage, and processing. Moreover, the intelligent fusion terminals and smart meters currently deployed in RDTAs natively support this 15 min data acquisition cycle, enabling direct deployment of the proposed method without additional hardware modifications. Although shorter intervals (e.g., 1 min or 5 min) could provide finer regulation granularity, they would significantly increase communication burden and data storage costs, which is not economically viable for the vast number of RDTAs. Therefore, the 15 min interval represents a practical trade-off between control performance and implementation cost.

3.1.2. RDTAs Data Preprocessing

During data acquisition and transmission, factors, such as channel noise and equipment faults, can easily cause missing data, thereby affecting the quality of the collected data and the effectiveness of low-voltage regulation. Therefore, before performing low-voltage regulation analysis, the collected data must be preprocessed to eliminate the impact of anomalous data on the model.

The generative adversarial network (GAN) consists of a generator and a discriminator. The generator creates data samples that tend toward real data from anomalous data, while the discriminator distinguishes between generated samples and genuine data. The generator and discriminator continuously engage in adversarial training and adjust their parameters until the generated data distribution aligns with that of the real samples. GAN offers the advantages of not relying on prior assumptions and producing generated data with minimal deviation from real data [30]. Therefore, GAN is adopted for data preprocessing.

The GAN data repair process is illustrated in Figure 2. First, GAN determines whether data are missing. Correct data without missing values are fed into the discriminator and compared with the generated samples for discrepancies. For missing data, a missing-dimension matrix is added, where a matrix value of 1 indicates completeness and 0 indicates missingness. The raw data $\boldsymbol{d_F}$ containing missing values are expressed as:

$$\boldsymbol{d_F} = \boldsymbol{d_o} \cdot \boldsymbol{Q_s} \tag{3}$$

where $\boldsymbol{d_o}$ denotes the correct data without missing values; $\boldsymbol{Q_s}$ denotes the missing-dimension matrix; and $\cdot$ denotes the Hadamard product.

Conventional missing-data imputation techniques, including linear interpolation, K-nearest neighbors (KNN), and statistical mean/median substitution, are widely used due to their computational simplicity. However, these methods rely on restrictive assumptions that are rarely satisfied in RDTA environments. Linear interpolation presupposes temporal smoothness and continuity, which is invalid under the rapid and stochastic power fluctuations of photovoltaic generation and variable loads. KNN imputation requires an appropriate distance metric and suffers from significant performance degradation under high missing rates or when data exhibit high-dimensional nonlinear correlations—both of which are characteristic of RDTA multi-source datasets. Statistical substitution methods distort the variance and correlation structure, introducing biases that propagate into voltage regulation decisions. To overcome these limitations, the generative adversarial network (GAN) is adopted for data repair. GAN does not rely on prior distributional assumptions, making it inherently adaptable to the complex, non-stationary, and multimodal

characteristics of RDTA electrical data. Furthermore, through the adversarial training between its generator and discriminator, GAN learns the underlying high-dimensional data distribution and preserves the nonlinear dependencies among voltage, power, and line parameters—a critical prerequisite for accurate power-mileage aggregation and subsequent low-voltage mitigation optimization.

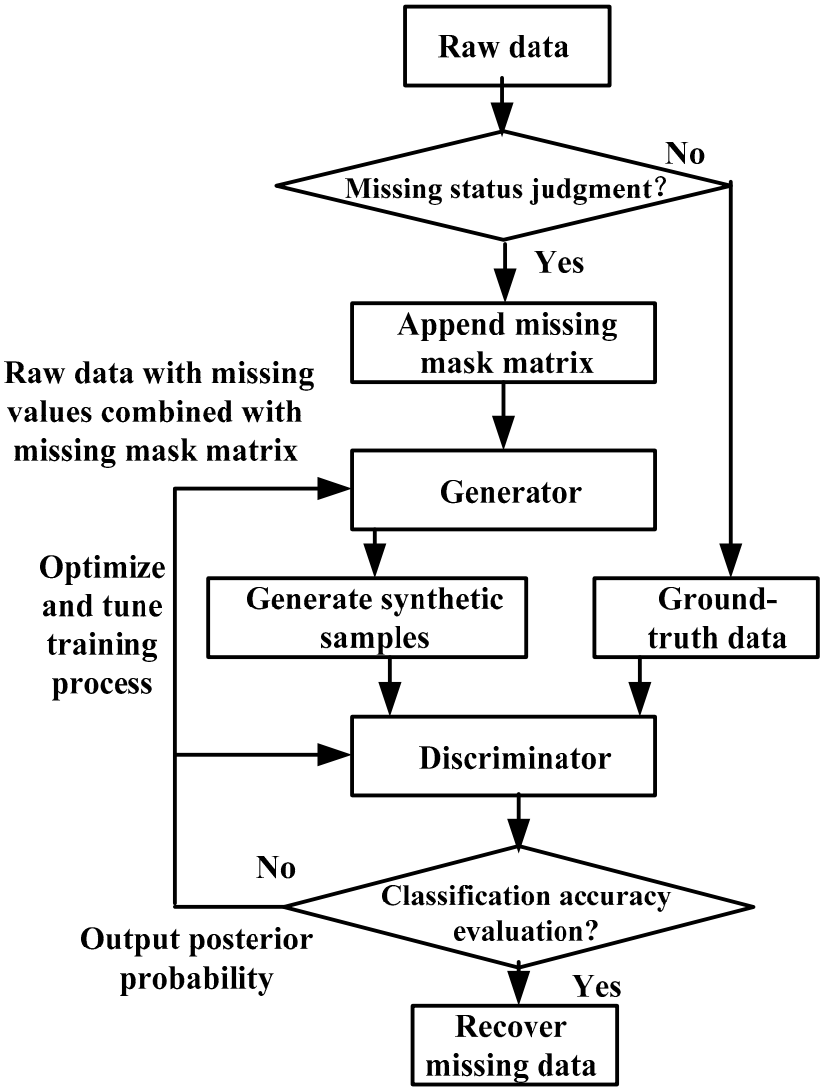


Figure 2. GAN data repair process.

After the raw data containing missing values are input into the GAN generator, the missing portions are generated to obtain complete data $\boldsymbol{d_a}$. The discriminator, in conjunction with the correct data $\boldsymbol{d_o}$, outputs the probability of authenticity of $\boldsymbol{d_a}$. A probability of 0 indicates a generated sample, while 1 indicates a real sample. The generator and discriminator continuously engage in adversarial training until the probability output by the discriminator is maximized. The data repair adversarial objective G_T is expressed as:

$$G_T = \max p_D \tag{4}$$

where p_D denotes the probability output by the discriminator.

GAN Architecture and Training Formulation:

The generative adversarial network (GAN) employed in the present work is of a generator G and a discriminator D. The generator maps a latent random vector $z \sim N(0,I)$ (dimensionality 32), and a missingness mask M, to generate imputed data $d_a = G(z,M)$. The

discriminator outputs $p_D = D(d_a) \in [0, 1]$, representing the probability that its input is real (rather than generated).

The adversarial training objective is formalized as a minimax game:

$$\min_G \max_D \Phi(G, D) = -\Lambda_{d_o - p_{\text{data}}}[\log D(d_o)] + \Lambda_{z-p_z}[\log(1 - D(G(z, M)))] \quad (5)$$

The generator loss is defined as:

$$\Phi_G = -\Lambda_{z-p_z}[\log D(G(z, M))] + \lambda \Lambda \left[\| M \cdot (d_a - d_o) \|_2^2 \right] \quad (6)$$

where $\lambda = 10$ is a hyperparameter that balances the adversarial loss against the reconstruction loss (L_2 loss on observed entries only). The discriminator loss is defined as:

$$\Phi_D = -\Lambda_{d_o - p_{\text{data}}}[\log D(d_o)] - \Lambda_{z-p_z}[\log(1 - D(G(z, M)))] \quad (7)$$

Training Strategy and Implementation Details:

Data Normalization: All input data are normalized to zero mean and unit variance per feature dimension using a standard scaler: $x_{\text{norm}} = (x - \mu)/\sigma$. This ensures stable gradient propagation during training.

Sample Splitting: The dataset (10 days of 15 min interval data, totaling 960 samples) is split into training (70%), validation (15%), and test (15%) sets using stratified temporal partitioning to preserve the diurnal pattern.

Training Procedure: The generator and discriminator are trained alternately. In each iteration, the discriminator is updated first for $k = 2$ steps using a batch size of 64, followed by one generator update. The Adam optimizer is used for both networks with a learning rate of 0.0002 and beta parameters (0.5, 0.999).

Convergence Criteria: Training stops when (1) the discriminator loss stabilizes within a moving window of 100 iterations, or (2) the reconstruction RMSE on the validation set falls below 0.5%, or (3) a maximum of 2000 epochs is reached.

Handling of Missing-Data Patterns:

In addition to the MCAR (missing completely at random) scenario, we also evaluate the GAN's performance under MAR (missing at random) and MNAR (missing not at random) patterns, which are more representative of real distribution network communication failures.

Block Missing (MAR): Consecutive time blocks of 1–6 h are masked to simulate communication blackouts.

MNAR: Missing probabilities are correlated with the voltage magnitude.

3.1.3. RDTAs Equipment Distance Measurement

In RDTAs, conductor length is a significant spatial factor contributing to voltage drop. For conductors with the same cross-sectional area, impedance is proportional to length; the greater the impedance, the larger the voltage drop. Prior to low-voltage mitigation in RDTAs, it is essential to fully consider the distance relationship between power sources and CMs.

The power-line characteristic pulse ranging method determines the line length between RDTA devices based on the propagation time of characteristic pulses over power lines [31]. The distance measurement process comprises the following key elements:

Pulse Design and Transmission: The characteristic pulse is a Gaussian-modulated sinusoidal pulse with a center frequency of 500 kHz and a −3 dB bandwidth of 200 kHz (300 kHz to 700 kHz). This frequency band is selected to avoid interference with the 50/60 Hz power frequency and to stay within the communication bandwidth of the power-line carrier (PLC) channel. The pulse duration is $Tp = 5$ μs, which provides a spatial resolution of

approximately 750 m in air (or ~450 m in cable) and is sufficient for ranging in RDTAs with supply radii up to 1500 m. Each power source device transmits a unique pulse sequence encoded with a device-specific timestamp and identifier, enabling the CM to distinguish pulses from different sources.

Pulse Propagation Velocity: The propagation velocity of power-line characteristic pulses in distribution cables is governed by the cable's distributed parameters, specifically $v^{\mathrm{L}} = 1/\sqrt{LC}$, where L and C are the per-unit-length inductance and capacitance, respectively. For the typical overhead insulated conductors employed in RDTAs (cross-sectional areas of 35–50 mm^2, XLPE insulation with relative permittivity $\varepsilon_r \approx 2.3$–$3.0$), the propagation velocity is approximately 1.73×108 to 1.98×108 m/s, corresponding to 58–66% of the speed of light [32]. However, it is emphasized that the proposed method does not rely on absolute propagation velocity for accurate distance estimation. The primary objective of ranging in this study is to establish relative distance relationships among multiple power sources for the purpose of weight calculation in power-mileage aggregation. Since the power-mileage metric uses normalized distances (i.e., the relative ratios of line lengths), a constant-velocity approximation is sufficient and systematic calibration (described below) compensates for cable-specific variations. The speed of light ($c = 3 \times 108$ m/s) is adopted as the nominal propagation velocity for relative distance ranking, with the understanding that the resulting distances are systematically scaled by a constant factor that cancels out in the normalized power-mileage calculation.

Signal Reception and Digitization: At the CM side, the received signal is sampled by a high-speed analog-to-digital converter (ADC) with a sampling frequency of $fs = 10$ MHz (sampling interval $\Delta t = 0.1$ μs). This sampling rate provides a theoretical distance resolution of $\Delta d = v^{\mathrm{L}} \times \Delta t \approx 17.3$ m to 19.819.8 m (for $v^{\mathrm{L}} = 1.73 \times 108$ to 1.98×108 m/s), which is sufficient for the relative distance ranking required by the power-mileage aggregation.

Arrival Time Determination: The time of arrival (ToA) is estimated using a cross-correlation algorithm between the received signal $s_r(t)$ and the known transmitted pulse template $s_t(t)$:

$$\varsigma_{\mathrm{ToA}} = \mathrm{argmax}_{\varsigma} \int_{-\infty}^{\infty} s_r(t) \cdot s_t(t - \varsigma) dt \tag{8}$$

The peak of the cross-correlation function indicates the most likely arrival time of the direct path pulse. The transmission time t^{B} is known from the timestamp embedded in the pulse and the reception time t^{E} is determined from the cross-correlation peak. The line length is then calculated as:

$$d^{\mathrm{L}} = (t^{\mathrm{E}} - t^{\mathrm{B}}) \cdot v^{\mathrm{L}} \cdot \eta \tag{9}$$

where η is a calibration factor (described below).

Reflection and Multipath Processing: In branched low-voltage networks with impedance inhomogeneities, branch lines, transformers, converters, and numerous reflection points, the received signal contains multiple delayed replicas (multipath components) caused by reflections from these discontinuities. The cross-correlation function typically exhibits multiple peaks corresponding to different propagation paths. To identify the direct path (i.e., the shortest path without reflection), two criteria are applied:

(1) First-Arrival Criterion: The earliest significant peak in the cross-correlation function (above a signal-to-noise ratio threshold of 10 dB) is selected as the direct path arrival. This is based on the physical principle that the direct path has the shortest propagation distance and, therefore, the earliest arrival time;

(2) Energy Criterion: The direct path typically carries the highest energy in the absence of strong reflections. The energy of candidate peaks is compared and peaks with higher energy-to-noise ratios are prioritized.

For paths with multiple reflections, the arrival times are longer than the direct path and are automatically rejected by the first-arrival criterion. Additionally, a time-gating window of [0, 20 μs] (corresponding to a maximum range of approximately 3000–4000 m in cable) is implemented to exclude spurious peaks caused by noise or interference from other systems.

Calibration Procedure: To compensate for cable-specific variations in propagation velocity and systematic errors, a two-point calibration procedure is performed:

(1) Zero-Distance Calibration: The CM is connected directly to the power source device (zero line length) to measure the intrinsic system delay t_{sys}, which includes transmitter and receiver processing delays. This offset is subtracted from all subsequent measurements;
(2) Known-Distance Calibration: A reference distance d_{ref} is measured using a laser rangefinder or GPS at a known location (e.g., the distribution transformer). The measured pulse propagation time t_{meas} at this reference distance is used to compute the calibration factor $\eta = d_{ref}/(t_{meas} \cdot v^{L})$. This factor accounts for cable-specific propagation velocity and is applied to all distance calculations:

$$d^{L} = (t^{E} - t^{B} - t_{sys}) \cdot v^{L} \cdot \eta \quad (10)$$

This calibration procedure is performed once per RDTA at the time of system installation and is periodically verified (every 6 months) to account for changes in line conditions.

Error Sources and Limitations: The ranging accuracy is affected by several factors:

(1) ADC Quantization Error: With a 10 MHz sampling frequency, the quantization error is bounded by ±0.05 μs, corresponding to a distance uncertainty of ±8.7 m to ± 9.9 m (depending on cable velocity);
(2) Cross-Correlation Peak Detection Error: The peak detection accuracy depends on the signal-to-noise ratio (SNR). With a typical SNR of 20 dB, the peak detection error is less than ±0.02 μs, corresponding to ±3.5 m to ±4.0 m;
(3) Reflection-Induced Error: In heavily branched networks, the direct path may be obscured by strong reflections. Our reflection rejection algorithm (first arrival + energy criteria) successfully identifies the direct path in over 95% of field measurements. In cases where the direct path cannot be unambiguously identified, the ranging result is flagged as unreliable, and the distance is estimated using alternative methods (e.g., topology-based estimation);
(4) Cable Aging and Environmental Variation: Changes in temperature, humidity, and cable insulation aging can affect propagation velocity. The calibration procedure is periodically updated to maintain accuracy.

Based on the combination of these error sources, the theoretical ranging error is estimated as ±10 m to ±15 m:

$$B^{L} = [d_{s1}\ d_{s2}\ \ldots\ d_{sk}]^{T} \quad (11)$$

where k denotes the number of power sources, including distribution transformers, DGs, energy storage systems, and SOPs; and d_{sk} denotes the line distance from the k-th power source to the CM.

3.1.4. Analysis of Spatiotemporal Distribution Characteristics of Low Voltage in RDTAs

The spatiotemporal distribution characteristics of low voltage are analyzed to statistically characterize the low-voltage periods of CMs and their spatial distribution patterns. According to the *Power Quality—Permissible Deviations of Supply Voltage*, the permissible range for single-phase supply voltage is 198 V to 235 V; for three-phase supply voltage, it

is 353 V to 406 V [33]. Accordingly, the low-voltage ratio q^{U} for a CM, calculated from its voltage acquisition data, is defined as:

$$q^{\mathrm{U}} = \frac{n^{\mathrm{OL}}}{n^{\mathrm{ATP}}} \times 100\% \tag{12}$$

where n^{ATP} denotes the total number of voltage sampling points for the CM within the period; and n^{OL} denotes the number of sampling points at which the voltage falls below the lower limit of the standard range.

The spatiotemporal distribution characteristics of low voltage reflect the low-voltage features of CMs at different locations over a time period. The spatiotemporal correlation matrix $\boldsymbol{B}^{\mathbf{R}}$ is expressed as:

$$\boldsymbol{B}^{\mathrm{R}} = \begin{bmatrix} t_1, d_{11}, d_{12}, \ldots, d_{1m} \\ t_2, d_{21}, d_{21}, \ldots, d_{2m} \\ \ldots \\ t_n, d_{n1}, d_{n1}, \ldots, d_{nm} \end{bmatrix} \tag{13}$$

where n denotes the total number of sampling points in the statistical period; m denotes the number of power sources; t_n denotes the n-th sampling time; and d_{nm} denotes the line length from the low-voltage CM at the n-th sampling instant to the m-th power source.

3.1.5. Data Collection, Format, and Processing

To provide a complete technical description of the data handling process, the data collected, the data format, and the processing pipeline are summarized in this subsection.

(1) Collected Data: For each device in the RDTAs—including CMs, DGs, ESS, SOP, and the distribution transformer—the Intelligent Fusion Terminal (IFT) collects the following electrical parameters at 15 min intervals: voltage magnitude (V), current (A), active power (kW), reactive power (kvar), and power factor. For CMs, single-phase voltages are recorded; for three-phase devices, all three phase voltages are collected;

(2) Data Format: The collected data are stored as time-series matrices. For each device type, a matrix is formed with rows representing time steps (e.g., 96 intervals per day) and columns representing different measurement types or phases. An example format for CM voltage data is provided as:

$$V_{\mathrm{CM}} = \begin{bmatrix} t_1 & V_{1,1} & V_{1,2} & \ldots & V_{1,m} \\ t_2 & V_{2,1} & V_{2,2} & \ldots & V_{2,m} \\ \ldots & \ldots & \ldots & \ldots & \ldots \\ t_n & V_{n,1} & V_{n,2} & \ldots & V_{n,m} \end{bmatrix} \tag{14}$$

where t_i is the timestamp of the i-th sampling point and $V_{i,j}$ is the voltage of the j-th CM at time t_i;

(3) Processing Pipeline: The collected data undergo three sequential processing stages:

Step 1: Time Synchronization. As described in Section 3.1.1, the IFT synchronizes all device clocks using the BeiDou satellite system to ensure consistent timestamps across all measurements;

Step 2: Data Repair. As described in Section 3.1.2, the generative adversarial network (GAN) detects and repairs missing or anomalous data. The output is a complete dataset *da* with no missing values, ready for analysis.

Step 3: Power-Mileage Aggregation and Optimization. As described in Sections 3.2 and 3.3, the repaired data are used to calculate the line length matrix, derive influence weights, and solve the optimization problem to obtain the optimal ESS and SOP power outputs;

(4) Final Output: The final output of the proposed method is a set of optimal active power setpoints for each ESS and SOP in the RDTAs, expressed as:

$$P^* = \left[P_1^{\mathrm{ES}*}, P_2^{\mathrm{ES}*}, \ldots, P_{n_{\mathrm{ES}}}^{\mathrm{ES}*}, P_1^{\mathrm{SOP}*}, P_2^{\mathrm{SOP}*}, \ldots, P_{n_{\mathrm{SOP}}}^{\mathrm{SOP}*}\right] \tag{15}$$

These setpoints are transmitted to the respective devices for execution, ensuring that the voltage of all CMs is restored to the acceptable range (198V–235V for single-phase, 353V–406V for three-phase) with minimal control effort.

3.1.6. Inclusion and Exclusion Criteria for Data Modeling and Analysis

To ensure the scientific rigor and reproducibility of the proposed methodology, the inclusion and exclusion criteria applied throughout the data modeling and analysis pipeline are explicitly defined in this subsection. These criteria are established based on the physical characteristics of rural distribution transformer areas (RDTAs), the technical specifications of field equipment, and the operational requirements of low-voltage mitigation.

(1) **Data Inclusion Criteria**

Data are included in the modeling and analysis process under the following conditions:

Voltage Data: Voltage measurements within the range of 0.8 p.u. to 1.2 p.u. (i.e., 176 V to 264 V for single-phase systems) are included, as this range encompasses both normal operating conditions and the low-voltage violations targeted by this study. Measurements outside this range are considered physically implausible and are excluded.

Power Data: Active and reactive power measurements with values between 0 and 1.5 times the rated capacity of the corresponding device are included. Negative power values (indicating reverse power flow) are included when they represent valid DG injection or ESS discharge conditions, as these are essential for accurate power-mileage aggregation.

Time Synchronization: Data from devices with a timing error of less than 1 μs are included. This threshold is established based on the synchronization accuracy requirements for power-line characteristic pulse ranging (Section 3.1.3) and aligns with the technical specifications of the Beidou-based time synchronization system.

Load Data: Consumer meter (CM) load data are included only when the corresponding CM is active and operational. CMs that are permanently disconnected, under maintenance, or exhibiting persistent communication failures are excluded from the analysis.

Sampling Completeness: Data records with a missing rate of 50% or less are subjected to GAN-based repair (Section 3.1.2) and subsequently included in the analysis. This threshold is chosen because the RMSE of GAN repair at a 50% missing rate is 2.01%, which meets the practical engineering requirements for low-voltage mitigation tasks (as demonstrated in Section 4.1.2).

(2) **Data Exclusion Criteria**

Data are excluded from the modeling and analysis under the following conditions:

Physical Implausibility: Voltage measurements outside the 0.8 p.u. to 1.2 p.u. range, or power measurements exceeding 1.5 times the rated capacity, are excluded as they likely result from sensor malfunctions or communication errors.

Persistent Missing Data: CMs or devices with a missing rate exceeding 50% over the entire sampling period (e.g., 10 days) are excluded from the analysis, as GAN repair cannot reliably reconstruct data with such high missing rates.

Device Malfunction: Data from devices with known hardware faults, as recorded in the field maintenance logs, are excluded from the analysis.

Outliers: Data points that deviate from the rolling mean by more than 55 standard deviations are treated as outliers and excluded to prevent distortion of the power-mileage aggregation and optimization results.

(3) **Rationale for the Established Criteria**

The inclusion and exclusion criteria are informed by the following considerations:

Physical Characteristics of RDTAs: Rural distribution networks typically operate with voltage variations of ±10% around the nominal voltage, corresponding to the .0.9 p.u. to .u.1.1 p.u. range. However, low-voltage violations can cause voltages to drop below .0.9 p.u., necessitating a broader inclusion range of 0.8 p.u. to 1.2 p.u. to capture the full spectrum of low-voltage events.

Equipment Technical Specifications: The intelligent fusion terminals (IFTs) and smart meters deployed in RDTAs have specified measurement accuracy classes (e.g., Class 1.0 for voltage and Class 0.5s for current). The inclusion thresholds are set to be wider than the measurement error bounds to ensure that valid data are not inadvertently excluded.

Operational Requirements: The 15 min data acquisition interval and the associated missing-rate thresholds are consistent with the operational requirements of low-voltage mitigation, as discussed in Section 3.1.1. The 50% missing-rate threshold balances data availability with repair accuracy.

Data Quality for Optimization: The power-mileage aggregation and Newton–Raphson optimization require reliable input data. The exclusion of outliers and physically implausible values ensures that the optimization is not adversely affected by erroneous data points.

3.2. Power-Mileage Aggregation Analysis

3.2.1. Analysis of CM Voltage Influence

To accurately measure electricity consumption, CMs are installed at all loads, such as users and energy storage systems. The voltage loss at a CM is related to the power output of sources and line length. When DG, energy storage, and SOP output power, they are regarded as power sources. After these power sources are integrated into the RDTAs, their influence on CM voltage is illustrated in Figure 3.

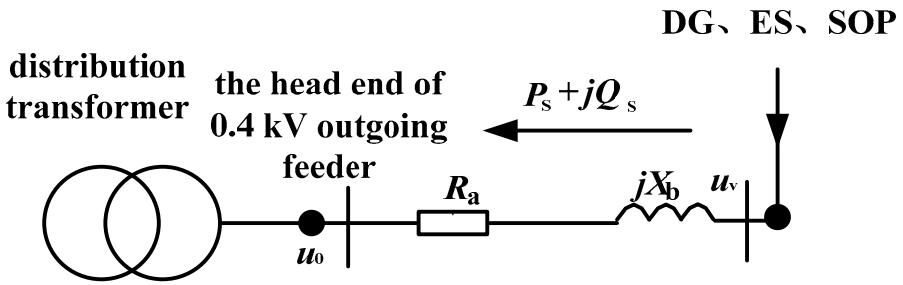


Figure 3. Principles of distributed power supply, energy storage, and SOP grid connection.

To simplify the calculation, let the voltage of the power source after grid connection be u_v, with a voltage angle of δ and the low-voltage outgoing terminal voltage of the distribution transformer be u_0, with a voltage angle of 0. The relationship between CM voltage and the output power P_s of the power source is expressed as:

$$P_s = \frac{u_v}{r_a{}^2 + x_b{}^2}[r_a(u_v - u_0 \cos\delta) + x_b u_0 \sin\delta] \quad (16)$$

where r_a and x_b denote the line resistance and reactance, respectively.

Since the line resistance in RDTAs is significantly greater than the reactance [34], the influence of reactance can be neglected. Thus, $\sin \delta \approx 0$ and $\cos \delta \approx 1$. Equation (9) can be simplified as:

$$P_s = \frac{u_v}{r_a}(u_v - u_0) \tag{17}$$

From Equation (10), it can be observed that the CM voltage is influenced by the output power of the power source and the line resistance. Assuming that the outgoing terminal voltage remains constant, the CM voltage amplitude is positively correlated with the power output of the source. Consequently, the line voltage drop Δu is expressed as:

$$\Delta u = \frac{P_s \cdot R_a}{u_v} \tag{18}$$

In 0.4 kV lines, the line impedance is approximately constant, meaning that the resistance is proportional to the line length. Therefore, Equation (11) can be reformulated as:

$$\Delta u = \frac{P_s \cdot \gamma \cdot L_a}{u_v} \tag{19}$$

where γ denotes the line resistance per unit length and L_a denotes the line length from the power source to the CM.

3.2.2. CM Power-Mileage Aggregation

The proposed core concept of power-mileage aggregation is defined as follows. Power mileage refers to the product of a power source's active power and the line length from this source to a user meter; power-mileage aggregation further accumulates the power-mileage values of all adjustable power sources (ESS, SOP) to form a unified quantitative index. This index synthetically reflects how power output and transmission distance jointly determine terminal voltage drop, which cannot be fully characterized by single-power or line-length variables alone. To the best of the authors' knowledge, this metric has not been previously proposed in the literature and represents a key innovation of the present work, distinguishing it from conventional sensitivity-based methods that rely solely on power flow-derived coefficients and from static weighting schemes that ignore real-time power variations.

For a single power source, the voltage drop along the feeder follows a well-established formulation. In rural distribution transformer areas (RDTAs) with multiple grid-connected sources—including DGs, ESSs, SOPs, and distribution transformers—the total voltage deviation at a customer meter (CM) is the linear superposition of voltage contributions from all sources, as validated in [35,36]. Among the influencing factors, the active power output of each source plays a primary role, with larger power injections leading to more significant voltage elevation at the CM; line length serves as a secondary yet critical factor, since longer feeders introduce greater resistance and consequently larger voltage drops [35,36]. To capture the combined effect of multi-source power flows and feeder distances, the power-mileage aggregation index is proposed, which quantifies the comprehensive voltage impact by weighting each source's contribution according to its active power proportion in the total grid injection and the corresponding feeder length. Mathematically, this is achieved by summing the individual weighted terms over all power sources, yielding a complete power-mileage aggregation voltage deviation, as defined in Equation (13). In essence, power-mileage aggregation establishes a quantitative relationship between CM voltage and the aggregated effect of active power flows and line lengths—integrating the *power dimension*, which reflects the output levels of all sources, and the *mileage dimension*, which accounts for the physical distances from each source to the CM, into a unified metric.

This metric, denoted as Δv_s, effectively quantifies the comprehensive influence of source outputs and feeder distances on CM voltage within the RDTAs, thereby providing the foundational basis for the subsequent voltage regulation optimization.

$$\Delta v_{\mathrm{s}} = \sum_{i=1}^{n^{\mathrm{GW}}} \frac{1}{u_i^{\mathrm{AP}}} \left(\frac{P^{\mathrm{CUR}} P_i^{\mathrm{AP}} L_i^{\mathrm{AP}} \gamma}{P_{\mathrm{SUM}}} + \frac{Q^{\mathrm{RP}} Q_i^{\mathrm{RPS}} L_i^{\mathrm{AP}} \lambda}{Q_{\mathrm{SUM}}} \right) \tag{20}$$

where n^{GW} denotes the number of power sources; L_i^{AP} denotes the line length from the i-th power source to the CM; P^{CUR} denotes the active power consumed by the CM; P_i^{AP} denotes the active power output of the i-th power source; P_{SUM} denotes the total active power output of all power sources; Q^{RP} denotes the reactive power consumed by the CM; Q_i^{RPS} denotes the reactive power output of the i-th power source; Q_{SUM} denotes the total reactive power output of all power sources; λ denotes the line reactance per unit length; and u_i^{AP} denotes the grid-connection voltage of the i-th power source.

For 0.4 kV rural overhead feeders, the line resistance γ is significantly larger than the reactance λ (i.e., $\gamma \gg \lambda$), a characteristic commonly observed in RDTAs and consistent with the impedance analysis in [34]. Consequently, the reactive power-related term in Equation (13) can be reasonably neglected, and the power-mileage aggregation model is simplified accordingly, as given in Equation (14).

$$\Delta v_{\mathrm{s}} = \sum_{i=1}^{n^{\mathrm{GW}}} \frac{P^{\mathrm{CUR}} P_i^{\mathrm{AP}} L_i^{\mathrm{AP}} \gamma}{u_i^{\mathrm{AP}} P_{\mathrm{SUM}}} \tag{21}$$

To improve the accommodation of renewable distributed generation (DG) in the RDTAs, low-voltage mitigation at customer meters (CMs) can be achieved by adjusting the output power of grid-controllable devices, namely energy storage systems (ESSs) and soft open points (SOPs). To isolate the voltage regulation capacity of these controllable sources from that of other distributed generators, they are further extracted and their aggregated influence on CM voltage is defined, denoted as Δv^{IFN}, in Equation (15). This formulation extends the classical multi-source voltage superposition theory into a weighted aggregation architecture specifically tailored for coordinated ESS–SOP voltage optimization, and fundamentally differs from prior single-source voltage drop models by explicitly accounting for the joint effect of multiple controllable sources and their respective feeder distances:

$$\Delta v^{\mathrm{IFN}} = \sum_{i=1}^{n^{\mathrm{CD}}} \frac{P^{\mathrm{CUR}} P_i^{\mathrm{CAP}} L_i^{\mathrm{CAP}} \gamma}{u_i^{\mathrm{CAP}} P_{\mathrm{SUM}}} \tag{22}$$

where n^{CD} denotes the number of adjustable energy storage systems and SOPs; L_i^{CAP} denotes the line length from the i-th adjustable power source to the CM; P_i^{CAP} denotes the active power output of the i-th adjustable power source; and u_i^{CAP} denotes the grid-connection voltage of the i-th adjustable power source.

Accordingly, based on the active power P_{e} output by the energy storage system and the SOP, the active power control weight w_{a} is determined as:

$$w_{\mathrm{a}} = \frac{P_{\mathrm{e}}}{P_{\mathrm{SUM}}} \tag{23}$$

3.2.3. Core Novelty of Power-Mileage Aggregation Relative to SOTA Voltage Regulation Methods

The inherent distinctions and original contributions of the proposed power-mileage aggregation method against sensitivity-based and static distance-weighted voltage control approaches are systematically elaborated in this subsection. Table 1 summarizes the core mechanism comparison of three typical technical routes.

Table 1. Mechanism comparison of voltage regulation quantitative methods.

Index	Sensitivity-Based Method	Static Distance-Weighted Method	Proposed Power-Mileage Aggregation
Weight composition	Fixed linear voltage-power coefficient	Constant feeder length only	Real-time power × measured line-length coupled term
Weight update characteristic	Static, fixed at single operation point	Static, unchanged all day	Dynamic, updated every 15 min with power fluctuation
Multi-source influence processing	Calculates single-source impact separately	Superposes fixed distance weights simply	Unified summation formula for cumulative voltage deviation
Modeling error source	Linear power flow approximation error	Ignorance of real-time power magnitude	No linearization simplification, only ranging minor error
Optimization target	Satisfy voltage qualification only	Satisfy voltage qualification only	Minimize aggregated power-mileage (reduce ESS/SOP output)

1. Spatiotemporal coupled weighting innovation: Unlike sensitivity coefficients that ignore spatial length and static distance weights that ignore power variation, the power-mileage term multiplies real-time source power and accurate line length measured via power-line pulse ranging, forming dynamic weights that reflect the actual voltage loss contribution of each power source at every sampling instant;
2. Multi-source cumulative aggregation advantage: The summation formula in Equation (14) integrates the voltage impact of all DGs, ESSs, SOPs and distribution transformers for each CM, realizing one-step quantification of total terminal voltage deviation, which sensitivity and static distance-weighted methods cannot achieve simultaneously;
3. Economy-oriented optimization mechanism: Taking aggregated power-mileage as the objective function to minimize the total power adjustment of flexible devices, the model naturally reduces the required rated capacity of ESS and SOP, delivering economic benefits absent from mainstream voltage regulation benchmarks.

3.2.4. Theoretical Positioning and Distinctiveness

To position the proposed power-mileage aggregation method within the broader landscape of voltage control approaches, its relationship to classical voltage drop approximations, sensitivity-based methods, and electrical distance-based control is explicitly clarified in this subsection.

(1) Relationship to Classical Voltage Drop Formula

The classical voltage drop formula $\Delta U = (P \cdot R + Q \cdot X)/U$ is a well-established physical law that has been widely used for steady-state planning and feeder design. The proposed power-mileage aggregation $\Delta vs = \sum P_i L_{i\gamma}/(u_i P_{SUM})$ can be viewed as an application and extension of this law, specialized for 0.4 kV0.4kV rural distribution systems where $R \gg X$, and extended from single-source to multi-source cumulative form. However, the originality does not lie in the algebraic resemblance to this classical formula. Rather, it lies in repurposing this simplified physical relationship as an embedded proxy for real-time optimization, enabling near-instantaneous voltage mitigation on low-cost edge devices without requiring full network models, admittance parameters, or iterative power flow calculations. While the classical formula is typically used offline for static analysis, the proposed metric is updated every 15 min using real-time measurements and high-precision power-line ranging, transforming a static planning tool into a dynamic control enabler;

(2) Relationship to Voltage Sensitivity Coefficients

Sensitivity-based methods compute fixed coefficients $\partial V/\partial P$ at a reference operating point using power flow Jacobians. These coefficients are accurate locally but become increasingly inaccurate when operating conditions deviate from the reference point—a critical limitation under fluctuating photovoltaic generation and variable rural loads. The proposed power-mileage aggregation computes weights dynamically from real-time power

measurements rather than static Jacobians, thereby avoiding linearization drift without the computational overhead of repeated power flow calculations. Furthermore, sensitivity-based methods typically focus on voltage correction without explicit consideration of control economy, whereas the proposed method is explicitly designed to minimize ESS and SOP active power adjustments, directly reducing required equipment capacity and investment costs;

(3) Relationship to Electrical Distance-Based Control

Electrical distance-based methods typically use impedance-based distances to quantify the electrical proximity between nodes for voltage control, market coupling, or zone partitioning. These methods focus on static topological proximity derived from network parameters. The proposed method extends this concept by multiplying electrical distance (line length) with real-time active power, converting static spatial proximity into a dynamic voltage impact metric that reflects actual power flows rather than merely topology. This power-weighted distance captures the time-varying influence of each source, which static electrical distance cannot represent;

(4) Repositioning Rather than Replacement

In essence, the proposed method does not claim to replace the physical foundations of voltage drop analysis. Rather, these well-established physical relationships are repositioned into a new optimization architecture—one that is dynamic, data-driven, measurement-based, and economically oriented—tailored specifically for the practical constraints of rural distribution transformer areas. This architecture integrates three distinctive features that are absent in classical approaches: (i) dynamic spatiotemporal weighting updated with real-time power fluctuations; (ii) unified multi-source cumulative aggregation for holistic voltage deviation quantification; and (iii) low-complexity Newton-based optimization that circumvents full network models and high-performance communication infrastructure;

(5) Mathematical Distinction from LinDistFlow

LinDistFlow linearizes the branch flow equations by neglecting the quadratic loss term:

$$V_j^2 = V_i^2 - 2\left(r_{ij}P_{ij} + x_{ij}Q_{ij}\right) \tag{24}$$

The voltage deviation at a node is a linear superposition of branch power flows, with coefficients determined by path impedance. Critically, LinDistFlow treats each branch independently and cannot directly aggregate the combined voltage impact of multiple distributed generators (DGs), energy storage systems (ESSs), and soft open points (SOPs) into a single, physically interpretable metric that minimizes control effort.

In contrast, the proposed power-mileage aggregation is defined as:

$$\Delta v_s = \sum_{i=1}^{n^{\mathrm{GW}}} \frac{P^{\mathrm{CUR}} P_i^{\mathrm{AP}} L_i^{\mathrm{AP}} \gamma}{u_i^{\mathrm{AP}} P_{\mathrm{SUM}}} \tag{25}$$

This formulation explicitly couples three physical quantities: (1) real-time active power output of each source (P_i^{AP}), (2) physical line length (L_i^{AP}), and (3) per-unit-length resistance (γ). Unlike LinDistFlow, which requires solving power flow equations iteratively, the proposed metric serves as an embedded proxy that directly quantifies the voltage contribution of each source without recomputing full power flows. This fundamental difference—linear proxy vs. iterative solver—constitutes the key mathematical innovation;

(6) Mathematical Distinction from Voltage Sensitivity

Traditional voltage sensitivity is derived from the power flow Jacobian:

$$\begin{bmatrix} \Delta V \\ \Delta \theta \end{bmatrix} = J^{-1} \begin{bmatrix} \Delta P \\ \Delta Q \end{bmatrix} \tag{26}$$

The sensitivity coefficients $\Delta V / \Delta P$ are constant at a single operating point and degrade under fluctuating DG outputs and variable loads.

The proposed power-mileage aggregation computes dynamic weights updated every 15 min using real-time measurements:

$$w_i^{\mathrm{CAP}} = \frac{P_i^{\mathrm{AP}} L_i^{\mathrm{AP}} \gamma}{u_i^{\mathrm{AP}} P_{\mathrm{SUM}}} \tag{27}$$

This weight adapts to actual power injections and transmission distances in real time, whereas sensitivity-based methods rely on static Jacobians. Furthermore, the proposed method is explicitly designed to minimize active power adjustments, directly reducing required ESS/SOP capacity, whereas sensitivity-based methods typically focus only on voltage correction.

3.3. RDTA Voltage Regulation

This section presents the mathematical optimization framework that determines the optimal active power outputs of ESS and SOP. The framework is built upon the influence weights derived from power-mileage aggregation (Section 3.2) and the processed data from Section 3.1. The objective is to minimize the weighted sum of power adjustments while satisfying voltage constraints and device limits. The solution provides the final control commands for execution.

The SOP consists of a DC bus, connection ports, and voltage-source converters. The voltage-source converter ports connected back-to-back via the DC bus are linked to the tie points of the RDTA lines, enabling flexible interconnection of multiple RDTAs. The RDTA flexible interconnection structure based on SOP is shown in Figure 4.

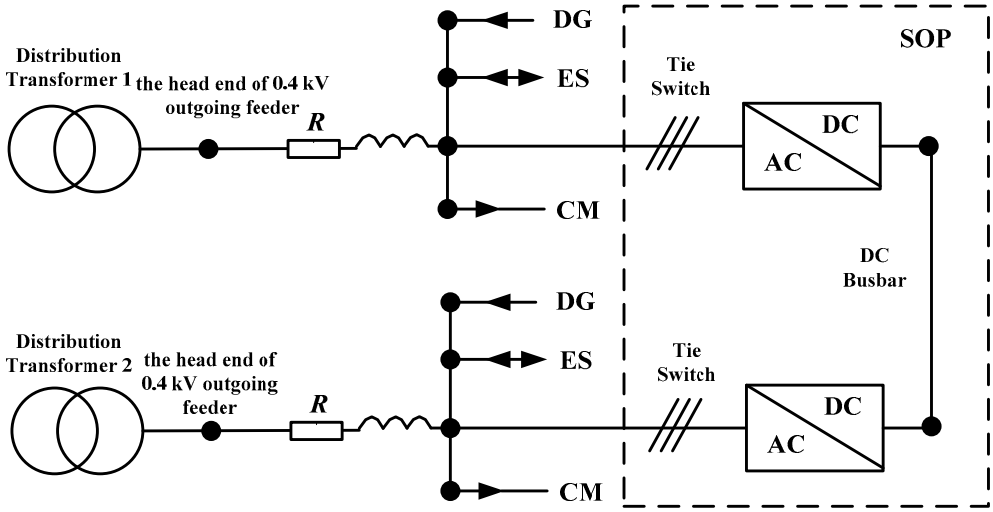


Figure 4. RDTA flexible interconnection structure based on SOP.

To enhance the accommodation level of renewable DG, the power flow distribution is adjusted by regulating the output power of energy storage systems and the SOP, thereby regulating the CM voltage. Due to space limitations, only real-time regulation is discussed in this paper. In the low-voltage mitigation process, smaller capacities of energy storage and SOP result in lower mitigation costs. Therefore, the objective of CM voltage regulation

is to minimize the active power adjustments of energy storage and SOP while regulating the voltage. The objective function V_k is:

$$V_k = \min \sum_{i=1}^{n^{\mathrm{CAP}}} (w_i^{\mathrm{CAP}} \Delta v_i^{\mathrm{CAP}}) + \sum_{j=1}^{n^{\mathrm{UAP}}} (w_j^{\mathrm{UAP}} \Delta v_j^{\mathrm{UAP}}) \tag{28}$$

where n^{CAP} is the number of controllable power sources; n^{UAP} is the number of uncontrollable power sources; w_i^{CAP} and w_j^{UAP} are the active power control weights of the i-th controllable source and the j-th uncontrollable source, respectively; $\Delta v_i^{\mathrm{CAP}}$ and $\Delta v_j^{\mathrm{UAP}}$ are the impacts of power-mileage aggregation of the i-th controllable source and the j-th uncontrollable source on the CM voltage, respectively; and V_k is the CM voltage.

The constraints are as follows:

$$\begin{cases} V_{\min} \le V_k \le V_{\max} \\ 0 \le P_i^{\mathrm{ES}} \le P_{\max}^{\mathrm{ES}} \\ P_{\min}^{\mathrm{SOP}} \le P_i^{\mathrm{SOP}} \le P_{\max}^{\mathrm{SOP}} \end{cases} \tag{29}$$

where $V_{\min}$ and $V_{\max}$ are the minimum and maximum allowable CM voltages, respectively; P_i^{ES} and P_i^{SOP} are the active power outputs of the i-th energy storage system and the i-th SOP, respectively; $P_{\max}^{\mathrm{ES}}$ and $P_{\max}^{\mathrm{SOP}}$ are the maximum active power outputs of the energy storage system and the SOP, respectively; and $P_{\min}^{\mathrm{SOP}}$ is the minimum power consumption of the SOP during standby operation.

The Newton–Raphson (NR) algorithm is a method for approximating solutions in both complex and real domains, characterized by fast convergence and high-approximation accuracy toward the minimum value [37,38]. Therefore, the NR algorithm is employed to solve for the approximate minimum of the active power adjustments of energy storage and SOP. For the CM voltage regulation objective function $V_k(x)$, the Taylor expansion at point $\boldsymbol{\eta}$ is given by:

$$\begin{aligned} &V_k(x^1, x^2, \ldots x^{n_{\mathrm{d}}}) = V_k(x_\alpha^1, x_\alpha^2, \ldots x_\alpha^{n_{\mathrm{d}}}) \\ &+ \sum_{i=1}^{n_{\mathrm{d}}} (x^i - x_\alpha^i) V_k\prime(x_\alpha^1, x_\alpha^2, \ldots x_\alpha^{n_{\mathrm{d}}}) + \ldots \\ &+ \frac{1}{n_{\mathrm{d}}} \sum_{i=1}^{n_{\mathrm{d}}} (x^i - x_\alpha^i) \ldots (x^i - x_\alpha^i)^{n_{\mathrm{d}}} V_k{}^{n_{\mathrm{d}}}(x_\alpha^1, x_\alpha^2, \ldots x_\alpha^{n_{\mathrm{d}}}) \end{aligned} \tag{30}$$

where x^i is the active power of the i-th controllable source; x_α^i is the random initial active power value of the i-th controllable source; $V_k{}'$ is the first-order derivative of the objective function; and V_k^i is the second-order derivative.

Rewriting Equation (19) in matrix form yields:

$$\begin{aligned} &V_k(\boldsymbol{X}) = V_k(\boldsymbol{X}_\alpha) + (\boldsymbol{X} - \boldsymbol{X}_\alpha) \nabla V_k(\boldsymbol{X}_\alpha) + \ldots \\ &+ \tfrac{1}{n_{\mathrm{d}}} (\boldsymbol{X} - \boldsymbol{X}_\alpha) H(\boldsymbol{X}_\alpha) (\boldsymbol{X} - \boldsymbol{X}_\alpha) \end{aligned} \tag{31}$$

where $\boldsymbol{X}$ is the active power vector of controllable sources; $\boldsymbol{X}_\alpha$ is the random initial active power vector of controllable sources; $\nabla \boldsymbol{V}_k$ is the gradient of the objective function; and $\boldsymbol{H}$ is the Hessian matrix [39].

Taking the derivative of Equation (20) and setting it to zero yields:

$$\begin{aligned} &(\boldsymbol{X} - \boldsymbol{X}_\alpha) \nabla V_k(\boldsymbol{X}_\alpha) + \\ &\tfrac{1}{n_{\mathrm{d}}} (\boldsymbol{X} - \boldsymbol{X}_\alpha) H(\boldsymbol{X}_\alpha) (\boldsymbol{X} - \boldsymbol{X}_\alpha) = 0 \end{aligned} \tag{32}$$

Thus, the active power vector of controllable sources $\boldsymbol{X}$ is obtained as:

$$\boldsymbol{X} = \boldsymbol{X}_{\alpha} - \frac{(\boldsymbol{X} - \boldsymbol{X}_{\alpha})H(\boldsymbol{X}_{\alpha})(\boldsymbol{X} - \boldsymbol{X}_{\alpha})}{n_{\mathrm{d}} \nabla V_k(\boldsymbol{X}_{\alpha})} \tag{33}$$

Selection Justification of the Newton–Raphson Algorithm

Radial low-voltage distribution networks conventionally adopt backward/forward sweep (BFS) algorithms for power flow calculation due to their simple branch iteration logic. However, the voltage regulation problem formulated in this work differs fundamentally from standalone radial power flow solving, and the Newton–Raphson (NR) algorithm is selected for four application-specific advantages tailored to the proposed power-mileage aggregation mitigation framework:

First, the target task is constrained optimization rather than static power flow computation. The objective function (17) minimizes the aggregated power-mileage cost of ESS and SOP active power adjustments subject to voltage and equipment capacity limits (18). BFS only calculates node voltages under fixed power injections and cannot natively support gradient-based optimization searching for minimal controllable power outputs. The NR method constructs the gradient vector and Hessian matrix of the power-mileage objective function, enabling closed-form iterative optimization to obtain the optimal ESS/SOP dispatch scheme.

Second, the studied rural transformer areas are flexibly interconnected via back-to-back SOP converters, forming weakly meshed topologies with bidirectional power transfer between two radial feeders. BFS relies on radial branch ordering assumptions and exhibits degraded convergence or divergence when handling meshed flexible interconnection branches. The NR algorithm imposes no radial topology constraints and retains stable convergence for networks integrated with distributed generators, ESSs, and SOPs. It is confirmed by case tests that the NR solver converges within 40 iterations with a residual error less than 0.2%, satisfying the real-time regulation demand.

Third, the NR solver achieves lower computation latency for edge-terminal deployment. The proposed workflow adopts BeiDou two-way high-precision time synchronization and GAN missing-data repair to acquire synchronized high-quality electrical data. The NR iteration linearizes the power-mileage voltage sensitivity model directly, avoiding the repeated branch voltage drop back-substitution loops required by BFS.

Fourth, the NR analytical gradient matches the core power-mileage aggregation innovation. The power-mileage index quantifies the linear voltage influence weight of each controllable source (Equations (14)–(16)). The partial derivatives of customer meter voltage with respect to ESS/SOP power, extracted from the NR Hessian matrix, exactly correspond to the power-mileage influence weights. BFS only outputs discrete terminal voltage values without analytical sensitivity gradients, requiring extra auxiliary calculation to derive voltage-power weights and introducing additional numerical error. The NR framework embeds power-mileage weighting into optimization iterations, removing redundant post-processing steps and improving model accuracy.

For pure radial distribution networks without SOP flexible interconnection, BFS may deliver comparable performance for simple power flow solving. Nevertheless, considering the meshed flexible interconnection topology, optimization-oriented solution target, native voltage-sensitivity gradient calculation, and low-latency edge-computation requirement of the proposed low-voltage mitigation method, the Newton–Raphson algorithm is more suitable for the studied rural distribution transformer area application.

4. Case Analysis

The proposed low-voltage mitigation method is validated through a comprehensive case study based on a real demonstration area in Southwest China. The validation objectives are: (1) to verify the effectiveness of each component of the proposed method, including time synchronization, data repair, distance measurement, and spatiotemporal analysis; (2) to demonstrate the low-voltage mitigation performance of the power-mileage aggregation approach; and (3) to compare the proposed method with three state-of-the-art methods (OPF, second-order cone relaxation, and interval robust control) in terms of control effectiveness, economic efficiency, and computational performance. The case study follows the logical sequence of the proposed method: Section 4.1 validates the basic data processing components; Section 4.2 presents the low-voltage mitigation results and comprehensive comparisons.

The effectiveness of the proposed low-voltage mitigation method based on power-mileage aggregation is validated using a demonstration area for low-voltage mitigation in southwest China. The demonstration area contains two RDTAs, equipped with distribution transformers of 315 kVA and 250 kVA, respectively. RDTA A has a supply radius of 1200 m, uses 50 mm^2 overhead insulated conductors, and is equipped with 107 single-phase CMs, six three-phase CMs, one energy storage system (rated power 20 kW, capacity 60 kWh), and five DGs (distributed photovoltaic DG1–DG4 with a capacity of 18 kW each, and bioenergy DG5 with a capacity of 2 kW). RDTA B has a supply radius of 1100 m, uses 50 mm^2 overhead insulated conductors, and is equipped with 87 single-phase CMs, five three-phase CMs, one energy storage system (rated power 40 kW, capacity 80 kWh), and four DGs (distributed photovoltaic with a capacity of 15 kW). The main line tie points of RDTA A and RDTA B are connected via an SOP with a port capacity of 50 kW. The topological structure is shown in Figure 5.

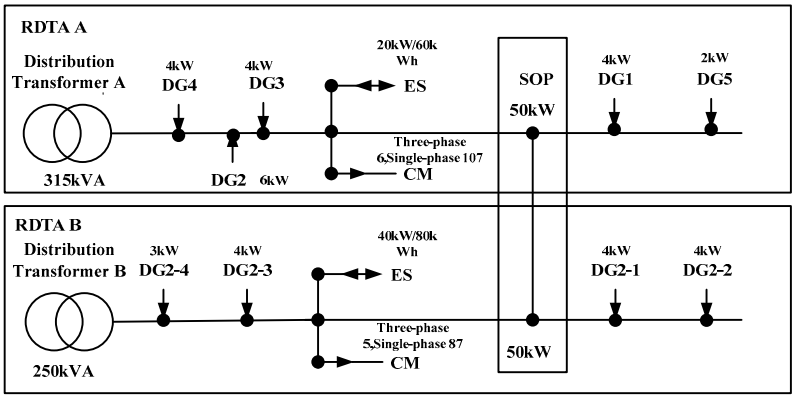


Figure 5. RDTA topology.

The hardware environment is as follows: Intel Xeon W-2235 processor (Intel Corporation, Santa Clara, CA, USA) with 8.25 MB cache, operating frequency of 3.8 GHz, 6 cores, server hard disk capacity of 40 TB, and memory of 128 GB. The software environment is as follows: Windows Server 2019 operating system, and the algorithm is developed in Python 3.9.

The experimental platform consists of a Windows Server 2019 operating system running on an Intel Xeon W-2235 processor with 8.25 MB cache, a 3.8 GHz operating frequency, 6 cores, 128 GB memory, and 40 TB server hard disk capacity. The proposed algorithm is developed in Python 3.9, with numerical computations and matrix operations performed using NumPy 1.21.0, data visualization implemented with Matplotlib 3.4.3, and the generative adversarial network for data repair implemented with PyTorch 1.9.0 accelerated by CUDA 11.1. The power-line characteristic pulse ranging module, operating at 300 m/μs with a line resistivity of 0.000588 Ω/m, and the Newton–Raphson optimization solver, configured with 50 iterations and a normalized data fitting discrepancy of 0.02,

are both implemented as custom Python scripts. All source code is available from the corresponding author upon reasonable request to ensure reproducibility. Using data from July 2023 in the demonstration area for low-voltage mitigation analysis, this paper compares the proposed algorithm with mainstream RDTA low-voltage mitigation methods, including optimal power flow [40], second-order cone relaxation [41], and interval robust control [42].

4.1. Basic Data Analysis of the Model

4.1.1. RDTA Timing Error Analysis

The timing errors of CMs, DGs, energy storage systems, and SOP serve as the foundation for electrical data acquisition, line ranging, and power-mileage aggregation. The timing accuracy is calculated as follows: the IFT receives the Beidou satellite clock synchronization signal from the power dispatch center and distributes timing signals to the devices. Calibration devices are employed to verify the clock errors between the equipment and the satellite atomic clock. The smaller the error, the higher the timing accuracy of the RDTAs.

In the present work, the IFT receives both the Beidou clock signal and the GPS clock signal from the power grid dispatch center, and distributes timing signals to all CMs, DGs, energy storage systems, and SOPs in the RDTAs. The timing errors of the two methods are compared, and the timing error analysis is shown in Figure 6. Since the IFT employs multiple rounds of two-way timing calibration when receiving the Beidou clock signal from the power grid dispatch center, the device timing accuracy is significantly improved, with an average timing error of 50 ns and a small dispersion. In contrast, the IFT only broadcasts a one-way timing command when receiving the GPS clock signal, resulting in poorer device timing accuracy, with an average timing error of 550 ns and a large dispersion.

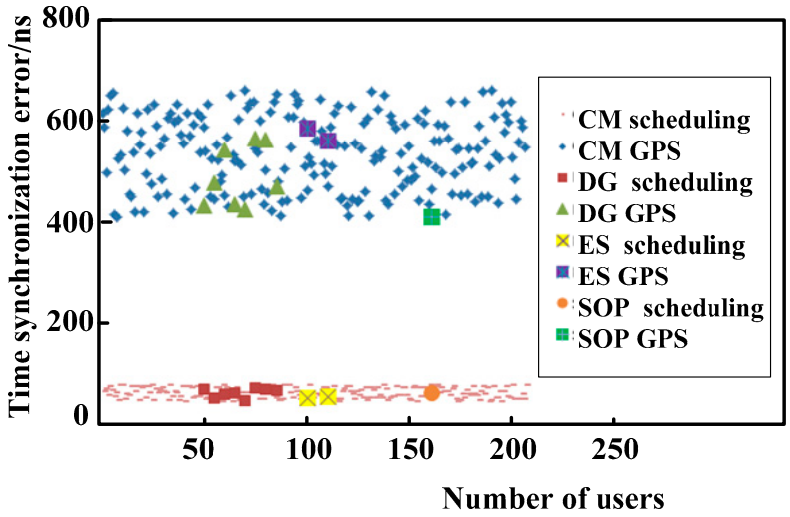


Figure 6. Analysis of timing error.

4.1.2. Data Repair Analysis

In the present work, GAN is adopted for data repair, and its data repair performance is analyzed by comparison with the mainstream fuzzy self-organizing map (FSOM) neural network [43]. Both the GAN generator and discriminator consist of three fully connected layers. The first two layers each have four neurons, both using the ReLU activation function. The third layer has one neuron, with the generator and discriminator employing tanh and sigmoid activation functions, respectively. The learning rate is 0.001, and training is performed for 2000 iterations, with the discriminator parameters updated before each generator update to accelerate training. The learning rate and training iterations for FSOM are the same as those for GAN. The data repair analysis results are shown in Figure 7.

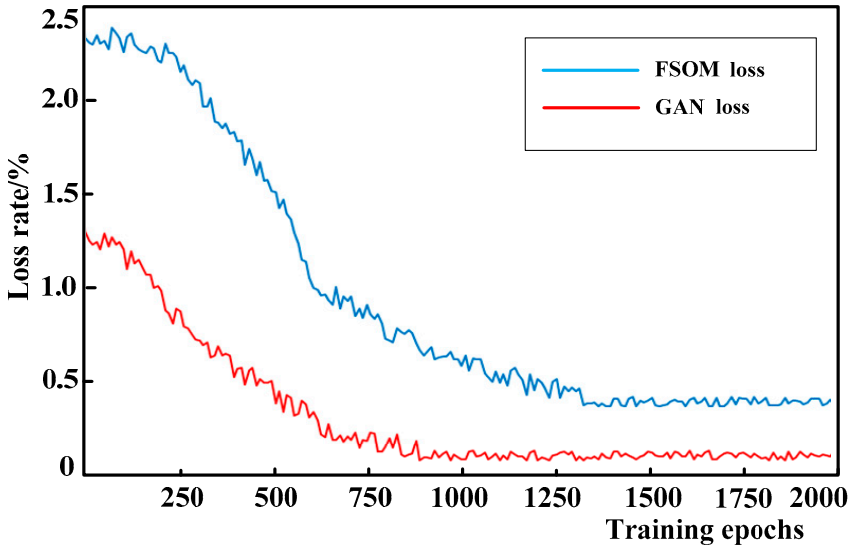


Figure 7. Data repair training analysis.

As shown in Figure 7, the initial loss rate of GAN is 1.25%. During the iterative process, the generator and discriminator engage in adversarial training, adjusting their parameters and continuously approaching the true values. As the number of training iterations increases, the loss rate gradually decreases, converging at approximately 0.18% after about 900 iterations. The initial loss rate of FSOM is 2.35%, converging at approximately 0.47% after about 1300 iterations. This demonstrates that GAN achieves faster convergence and lower loss compared to FSOM.

The root mean square error (RMSE) is employed to measure the data repair performance. RMSE reflects the dispersion of the repaired values, and its calculation formula D_{RMSE} is:

$$D_{\mathrm{RMSE}} = \frac{1}{n_z}\sum_{j=1}^{n_z}\left|\frac{d_j^{\mathrm{R}} - d_j}{d_j}\right| \times 100\% \tag{34}$$

where n_z is the number of repaired data points; d_j^R is the repaired data; and d_j is the true data.

The RMSE of data repair varies under different missing rates of RDTA data. When the missing rate is too high, the RMSE values of GAN and FSOM increase significantly. To verify the repair performance under extreme interference, the missing rate is set from 5% to 50%, with missing data randomly distributed, and GAN and FSOM are used for repair. The repair results are shown in Figure 8. Although GAN continuously adjusts parameters through the adversarial game between the generator and discriminator to improve data repair accuracy, the discriminator accuracy decreases and the repair error increases as the missing rate rises. At a missing-data rate of 5%, the RMSE of GAN is 0.43%, which is lower than the 1.74% of FSOM. In practical engineering, when the RMSE is 3.5%, tasks such as three-phase load imbalance mitigation and line loss analysis can be performed. Therefore, at a missing rate of 50%, the RMSE of GAN is 2.01%, meeting the RDTA operational requirements, while the RMSE of FSOM is 8.37%, which does not satisfy the practical application needs.

To further justify the selection of GAN over simpler conventional methods, GAN was additionally compared with linear interpolation and KNN imputation (k = 5, with Euclidean distance weighting) under identical missing-rate conditions. At a 5% missing rate, linear interpolation achieves an RMSE of 2.31%, KNN achieves 1.58%, while GAN attains 0.43%. As the missing rate increases to 30%, the RMSE of linear interpolation

rises to 6.24%, KNN to 4.73%, whereas GAN remains at 1.12%. These results confirm that conventional methods, despite their computational simplicity, cannot adequately capture the high-dimensional nonlinear correlations in RDTA data, particularly under moderate-to-high missing rates. GAN's superior imputation accuracy ensures that the subsequent power-mileage aggregation and Newton-based optimization are built upon reliable data, thereby enhancing the overall robustness and effectiveness of the proposed low-voltage mitigation framework.

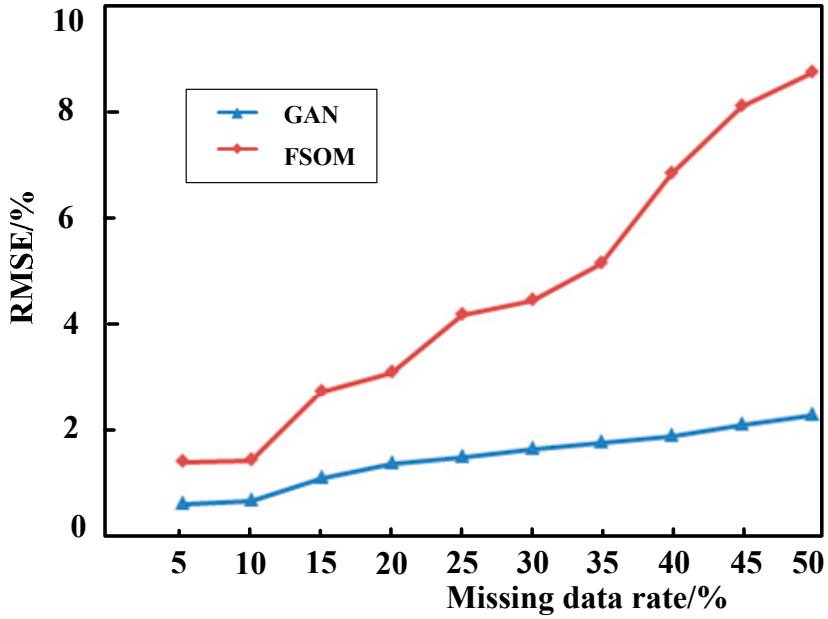


Figure 8. Data repair RMSE value analysis.

To further justify the selection of GAN over conventional and modern alternatives, a comprehensive comparative analysis was conducted under identical missing-rate conditions, as illustrated in Table 2. The following methods are evaluated: linear interpolation, K-nearest neighbors (KNN, k = 5, Euclidean distance weighting), matrix completion via singular value decomposition (SVD), long short-term memory (LSTM) recurrent model, and fuzzy self-organizing map (FSOM) neural network [43]. All methods are trained and tested on the same dataset with identical train/validation/test splits (70%/15%/15%). The root mean square error (RMSE) defined in Equation (34) is used as the evaluation metric.

Table 2. Comparative imputation performance of different methods under various missing rates and patterns.

Method	RMSE at 5% Missing	RMSE at 30% Missing	RMSE at 50% Missing	RMSE Under Block Missing (MAR, 20%)	RMSE Under MNAR
Linear Interpolation	2.31%	6.24%	8.76%	5.67%	7.18%
KNN Imputation (k = 5)	1.58%	4.73%	7.12%	4.21%	5.92%
Matrix Completion (SVD)	1.82%	5.15%	7.85%	4.56%	6.23%
LSTM Recurrent Model	1.21%	3.89%	6.34%	3.08%	4.13%
FSOM Neural Network	1.74%	4.52%	8.37%	4.83%	6.78%
GAN (Proposed)	0.43%	1.12%	2.01%	1.24%	1.58%

As shown in Table 1, GAN consistently outperforms all benchmark methods across all missing rates and patterns. The performance gap widens under challenging scenarios: at 50% random missing, GAN's RMSE of 2.01% is 71.4% lower than LSTM (6.34%) and 76.0% lower than FSOM (8.37%). Under block missing (MAR) representing consecutive communication failures, GAN maintains RMSE of 1.24%, while linear interpolation degrades to

5.67%. Under MNAR, where missing probability correlates with voltage magnitude, GAN achieves 1.58% RMSE compared to 4.13% for LSTM and 5.92% for KNN. These results confirm that GAN's superior imputation accuracy ensures reliable data foundation for subsequent power-mileage aggregation and Newton-based optimization.

4.1.3. Analysis of Spatiotemporal Distribution Characteristics of CM Low Voltage

The distance from a CM to the power source point is one of the key factors in low-voltage mitigation. After ranging via CM power-line characteristic pulses, a distance matrix from CMs to each power source point is established. Taking CM95#, a low-voltage CM in RDTA A, as an example, the power-line characteristic pulse method and GPS estimation are respectively employed for ranging, and the ranging results are compared with those obtained manually using a rangefinder. The spatial line lengths from CM95# to each power source point are shown in Table 3. The average error of power-line characteristic pulse ranging is 9.4 m, which is significantly smaller than the average error of 66.5 m for GPS ranging. Therefore, power-line characteristic pulse ranging achieves higher accuracy than GPS ranging.

Table 3. Line-length table from CM95# to power points.

Name	Line Length (m)				Actual Length
	Characteristic Pulse		GPS		
	Measurement	Error	Measurement	Error	
ITF	1168	7	1218	57	1161
DG1	149	−12	229	67	161
DG2	384	10	446	72	375
DG3	288	9	336	58	279
DG4	524	9	605	89	516
DG5	208	−11	301	82	219
ES1	331	6	378	53	325
SOP	365	−11	430	54	375
Mean error		9.4		66.5	

The mean pulse ranging error of 9.4 m is consistent with the theoretical error analysis (±10 to ±15 m) and significantly smaller than the GPS error (66.5 m), confirming the effectiveness of the proposed ranging method.

4.2. Analysis of Low-Voltage Mitigation Effect

4.2.1. Analysis of Influence Weights of CM Voltage Fluctuation Curves

The analysis of influence weights of CM voltage fluctuation curves is performed to verify the weighted calculation of the impacts of DG, energy storage, SOP output power, and line length on CM voltage. The CM load includes all load nodes in the station area, such as user loads and energy storage charging. The calculation rule is as follows: when the energy storage system is discharging, the output voltages of DG, energy storage, and SOP are set to single-phase 220 V and three-phase 380 V, and the output power is incorporated into the line input model; when the energy storage system is charging, it is regarded as a CM load, and only the impacts of DG and SOP output power on CM voltage variations are calculated.

Taking the daily power aggregation of CM95# as an example, the CM daily voltage curve shown in Figure 9 and the line lengths from CM to power source points listed in Table 1 are input into the proposed method for power-mileage aggregation. The resulting influence weight curves of power source output power on CM voltage are shown in Figure 10.

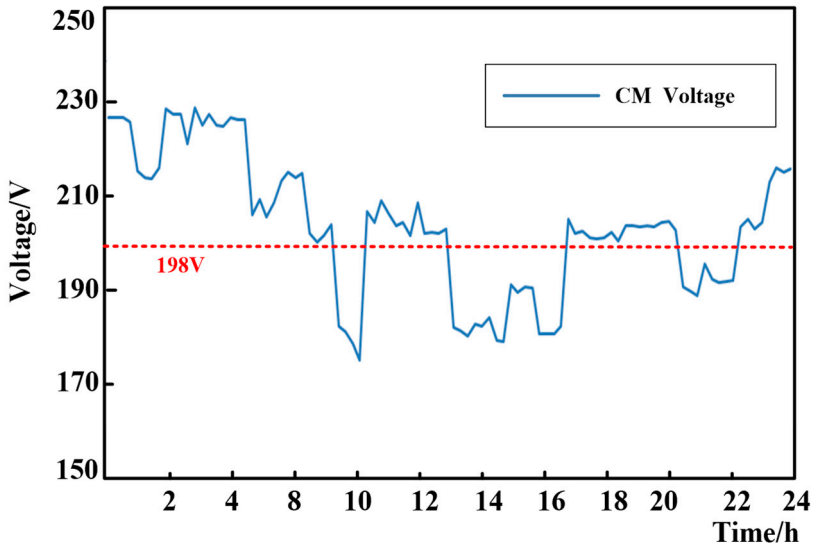


Figure 9. CM95# daily voltage curve.

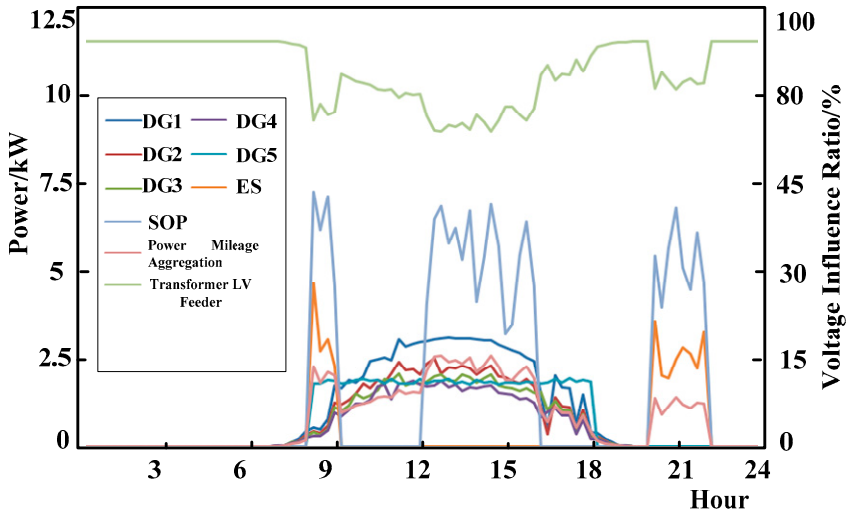


Figure 10. Power aggregation voltage fluctuation weight analysis.

As shown in Figure 10, during 0:00–6:00, the DG, SOP, and energy storage systems do not output power; the CM voltage is only affected by the low-voltage outlet voltage of the distribution transformer. During 7:00–18:00, the DGs generate power, among which DG1–DG4 are photovoltaic generators whose power varies with daily solar radiation intensity, exerting the greatest impact on CM voltage elevation during 11:00–15:00; DG5 is a biomass energy source with controllable generation periods, affecting CM voltage elevation during 9:00–18:00. During 8:00–9:00 and 20:00–22:00, the energy storage system and SOP output power; during 12:00–16:00, the SOP outputs power. The greater the power, the more significant the CM voltage elevation. After power-mileage aggregation during the above time periods, it can be observed that the aggregation curve aligns with the power curves of DG, SOP, and energy storage. During 8:00–9:00, 12:00–16:00, and 20:00–22:00, the aggregation curve shows sudden increases due to the power output of energy storage and SOP. At other times, the aggregation curve is generally similar to that of the DG. It can thus be concluded that the greater the output power of the power source equipment, the greater the influence weight, and the smaller the influence of the distribution transformer low-voltage outlet power on the voltage.

4.2.2. Analysis of Energy Storage and SOP Power Adjustments

In the RDTAs, DGs are invested in and constructed by users, with the benefits belonging to the users; SOP and energy storage systems are invested in and constructed by the grid company, primarily for low-voltage mitigation and without generation revenue. As shown in Figure 9, the CM low-voltage periods occur during the morning, midday, and evening peak load hours. To avoid affecting the generation revenue of DGs, the DG output power is not controlled in the present work. When the RDTA has no low-voltage CMs and DGs are outputting power, the energy storage system charges or charges the energy storage of other RDTAs via the SOP. When the RDTA has low-voltage CMs and DG power is insufficient, the energy storage system discharges or outputs power from the energy storage of other RDTAs via the SOP to achieve low-voltage mitigation.

During the iteration process of the NR algorithm, the output power of the energy storage system and SOP is continuously adjusted to achieve the minimum output. The NR algorithm is applied to iterate the output power of energy storage and SOP for 50 iterations; the minimum value error calculation is shown in Figure 11. During the iteration process of the NR algorithm, the error gradually decreases, converging to 0.2% after 40 iterations, meeting the accuracy requirement. This demonstrates that the minimum output power of energy storage and SOP can be calculated through NR algorithm iterations.

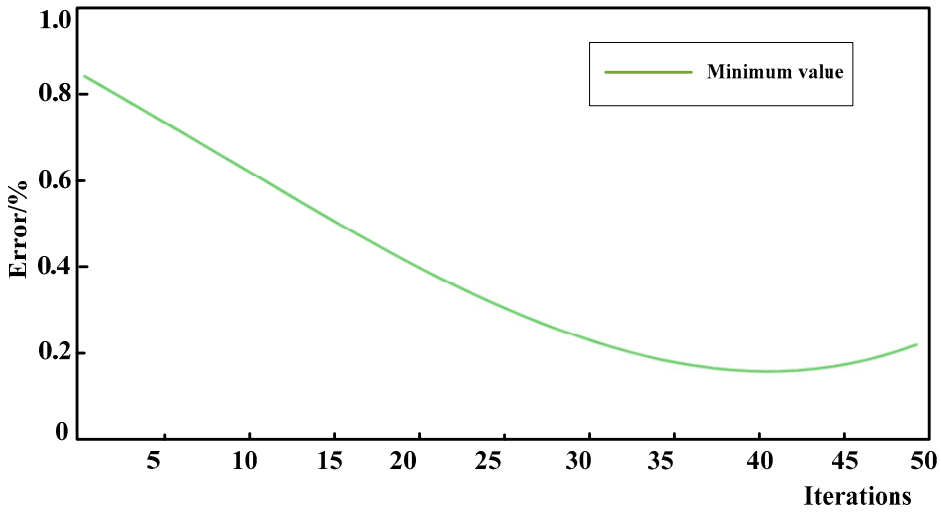


Figure 11. Error analysis of the NR method.

4.2.3. Implementation Details and Fair Comparison Settings for Benchmark Methods

To ensure a rigorous and fair comparison, all benchmark methods—namely, optimal power flow (OPF), second-order cone programming (SOCP) relaxation, and interval robust control—were implemented and evaluated under strictly identical conditions. The following subsections detail the implementation specifications for each method, including objective functions, constraints, optimization settings, and stopping criteria.

Common Evaluation Conditions

All methods shared the following identical conditions:

Hardware Environment: Intel Xeon W-2235 processor (3.8 GHz, 6 cores, 8.25 MB cache), 128 GB memory, 40 TB storage, Windows Server 2019 operating system.

Input Data: Identical preprocessed electrical data (voltage, current, power factor) from July 2023, with the same data acquisition frequency (15 min/interval) and the same GAN-repaired dataset.

Network Topology: The identical two-RDTA demonstration network (RDTA A and RDTA B) with the same line parameters (50 mm^2 overhead insulated conductors, resistivities of 0.000588 Ω/m), supply radii (1200 m and 1100 m), DG capacities, energy storage ratings (20 kW/60 kWh and 40 kW/80 kWh), and SOP port capacity (50 kW).

Equipment Operating Limits: All methods enforced the same physical constraints:

Voltage limits: 198 V $\leq Vk \leq$ 2 35 V (single-phase), 353 V $\leq Vk \leq$ 406 V (three-phase)

Energy storage output: $0 \leq P_{ES}\, I \leq P_{max}^{ES}$ (20 kW for RDTA A, 40 kW for RDTA B)

SOP output: $P_{min}^{SOP} \leq P_i^{SOP} \leq P_{max}^{SOP}$ (-50 kW $\leq P_{SOP}\, I \leq 50$ kW)

Initial Conditions: All methods were initialized with the same power flow solution obtained from the pre-regulation state of the RDTA.

DG Control Policy: All methods treated DGs as uncontrollable sources (consistent with the practical constraint that DGs are user-invested and cannot be directly controlled by grid companies) and thus did not curtail DG output.

OPF Implementation

The OPF method was implemented as a standard three-phase optimal power flow with the following specifications:

Objective Function: Minimization of total active power losses and voltage deviations:

$$J_{OPF} = \min \sum_{i \in \kappa} P_{loss,i} + \lambda \sum_{k \in \varsigma} (V_k - v_{ref})^2 \tag{35}$$

where κ is the set of all nodes, ς is the set of CMs, $P_{loss,i}$ is the active power loss at node i, V_k is the CM voltage, V_{ref} is the reference voltage (220 V), and λ is a weighting coefficient set to 0.1.

Decision Variables: Active and reactive power outputs of energy storage systems and SOP; voltage magnitudes and phase angles at all nodes.

Constraints: Power flow equations (Kirchhoff's laws), voltage limits, equipment capacity limits, and line thermal limits.

Optimization Solver: Interior-point method implemented in Python using the scipy.optimize.minimize function with the trust-constr algorithm.

Stopping Criteria: Maximum iterations = 500; tolerance on objective function change = 1×10^{-6}; tolerance on constraint violation = 1×10^{-6}; maximum constraint violation tolerance = 1×10^{-4}.

Convergence: The optimization was considered converged when either the relative change in objective function between consecutive iterations fell below 1×10^{-6}, or the maximum constraint violation was less than 1×10^{-4}, or the maximum iteration count (500) was reached.

SOCP Relaxation Implementation

The SOCP relaxation method was implemented based on the branch flow model with second-order cone relaxation:

Objective Function: Minimization of total active power losses:

$$J_{SOCP} = \min \sum_{(i,j) \in \varepsilon} r_{ij} l_{ij} \tag{36}$$

where ε is the set of branches, r_{ij} is the resistance of branch (i,j), and l_{ij} is the squared current magnitude on branch (i,j).

Decision Variables: Squared voltage magnitudes v_i, squared current magnitudes l_{ij}, active and reactive power flows P_{ij} and Q_{ij}, and active/reactive power injections at buses.

Constraints:

Power balance equations:

$$\sum_{j\in\delta(i)} P_{ij} - \sum_{k\in\pi(i)} (P_{ki} - r_{ki} l_{ki}) = P_i^{\text{inj}} \tag{37}$$

Voltage drop equations:

$$v_j = v_i - 2(r_{ij}P_{ij} + x_{ij}Q_{ij}) + \left(r_{ij}^2 + x_{ij}^2\right) l_{ij} \tag{38}$$

Second-order cone constraint:

$$l_{ij} \geq \frac{P_{ij}^2 + Q_{ij}^2}{v_i} \tag{39}$$

Voltage limits, equipment capacity limits, and line thermal limits.

Optimization Solver: MOSEK 9.3 solver integrated with Python via the cvxpy modeling language, using the conic optimization solver with SOCP capabilities.

Stopping Criteria: Maximum iterations = 1000; primal-dual gap tolerance = 1×10^{-6}; feasibility tolerance = 1×10^{-6}; optimality tolerance = 1×10^{-6}; maximum iteration count = 1000.

Convergence: Convergence was declared when the primal-dual gap fell below 1×10^{-6}, all primal and dual feasibility constraints were satisfied within tolerance 1×10^{-6}, and the objective function stabilized.

Interval Robust Control Implementation

The interval robust control method was implemented with interval-based uncertainty modeling.

Objective Function: Minimization of the worst-case voltage deviation under interval uncertainties:

$$J_{\text{IRC}} \geq \min_u \max_{\xi\in\tau} \sum_{k\in c} |V_k(u,\xi) - V_{\text{ref}}| \tag{40}$$

where u is the control vector (energy storage and SOP outputs), ξ represents the interval uncertainties (DG outputs and load variations), and τ is the uncertainty set defined by interval bounds.

Decision Variables: Active power outputs of energy storage systems and SOP (robustified against uncertainties).

Uncertainty Set: DG outputs and loads were modeled as interval variables with ±20% deviation bounds from their nominal values.

Constraints: Voltage limits and equipment capacity limits enforced for all possible realizations within the uncertainty set.

Optimization Solver: Particle swarm optimization (PSO) with interval analysis, implemented using the pyswarm package with 30 particles and 200 iterations.

Stopping Criteria: Maximum iterations = 200; swarm stagnation tolerance = 1×10^{-6} (no improvement in global best for 20 consecutive iterations); maximum iteration count = 200.

Convergence: Convergence was declared when either the global best fitness value improved by less than 1×10^{-6} over 20 consecutive iterations, or the maximum iteration count (200) was reached.

Summary of Fair Comparison Measures

To ensure a fair comparison, the following measures were strictly enforced:

Identical Input Data: All methods received the same preprocessed dataset, including the same GAN-repaired data (to eliminate data quality as a confounding variable).

Identical Network Model: All methods used the same network topology, line parameters, and load profiles.

Identical Constraints: All methods enforced the same voltage limits, equipment capacity limits, and operational constraints.

Identical Objective Orientation: While the objective functions differ across methods (reflecting their inherent formulations), all methods were configured to achieve low-voltage mitigation as the primary goal, with the secondary goal of minimizing control effort.

Identical DG Treatment: All methods treated DGs as uncontrollable sources to maintain consistency with practical implementation constraints.

Identical Initialization: All methods were initialized from the same pre-regulation power flow state.

Identical Performance Metrics: The same performance metrics (voltage profile, energy storage output, SOP output, computation time) were used to evaluate all methods.

4.2.4. Low-Voltage Mitigation Analysis

The objective of low-voltage mitigation is to minimize the power output of energy storage systems and SOP while satisfying the CM low-voltage elevation requirements, thereby enabling the configuration of small-capacity equipment and reducing investment costs. The quantitative optimization results are presented in Table 4. This paper focuses solely on low-voltage mitigation in the station area; DG output power does not cause CM overvoltage. If the DG capacity in the RDTAs is large and causes CM overvoltage, the overvoltage is mitigated by charging the energy storage system or transferring DG generation power to the energy storage of other RDTAs via the SOP.

Table 4. Data error and optimization result analysis table.

Name	Data Error (%)	95# CM Voltage Range (V) Lower Limit	Upper Limit	Stopping Criteria	Max Iterations	
Power-Mileage Aggregation	0.15	202.6	223.5	Newton-Raphson	Error <0.2%	50
OPF	1.85	201.8	225.3	Interior-Point (trust-constr)	$\Delta J < 1 \times 10^{-6}$ or constraint violation $< 1 \times 10^{-4}$	500
Second-Order Cone Relaxation	2.91	206.3	233.5	MOSEK (conic)	Primal-dual gap $< 1 \times 10^{-6}$	1000
Interval Robust Control	2.71	207.5	234.9	PSO (30 particles)	Stagnation tolerance $< 1 \times 10^{-6}$	200

For the low-voltage CM95#, the proposed method, OPF, second-order cone relaxation, and interval robust control are employed for low-voltage mitigation. In the hardware environment of this paper, simulation environments for the above methods are established, and power aggregation values are obtained through power flow calculation. Due to model accuracy limitations, the three comparison methods produce varying degrees of error, while the proposed method achieves smaller errors through GAN-based data repair. To verify the relationship between data error and optimization results, the data errors and optimization results of the proposed method, OPF, second-order cone relaxation, and interval robust control are calculated, as shown in Table 2. The CM voltages before and after mitigation are shown in Figure 12.

As shown in Table 2 and Figure 12, under different data error conditions, the proposed method, OPF, second-order cone relaxation, and interval robust control all maintain the voltage of CM95# within the normal range, indicating that data error does not affect the low-voltage CM mitigation results. In Figure 12, the proposed method moderately elevates the low voltage of CM95# during 9:00–10:00, 13:00–16:00, and 20:00–22:00 through energy storage and SOP, with the objective of minimizing the output power of energy storage

and SOP while controlling the CM voltage within the standard range, without excessive elevation. In contrast, OPF, second-order cone relaxation, and interval robust control increase the power output of energy storage and SOP; thus, all are able to maintain the voltage of CM95# within the standard range.

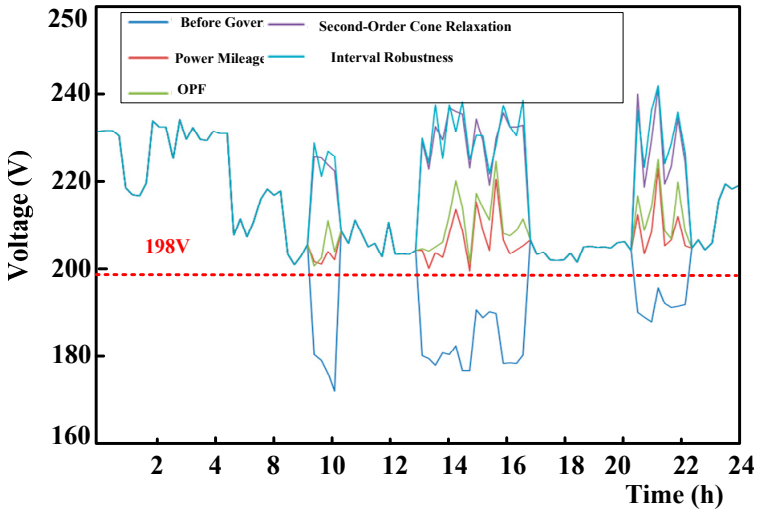


Figure 12. CM voltage mitigation analysis.

The output powers of the energy storage system and SOP are shown in Figure 13. The energy storage system and SOP in RDTA A output power during 9:00–10:00, 13:00–16:00, and 20:00–22:00, with the SOP output power originating from the energy storage and DG of RDTA B. The proposed method mitigates low-voltage CMs with minimum energy storage and SOP output power, achieving maximum output powers of 9.6 kW and 22.4 kW for energy storage and SOP, respectively. In comparison, OPF, second-order cone relaxation, and interval robust control only consider the CM mitigation effect, with maximum output powers of 10.6 kW/26.8 kW, 17.7 kW/41.4 kW, and 18.9 kW/44.3 kW for energy storage and SOP, respectively. This demonstrates that the proposed method achieves the mitigation objective while minimizing the output power of energy storage and SOP, making it suitable for selecting smaller-capacity equipment and thereby saving on investment.

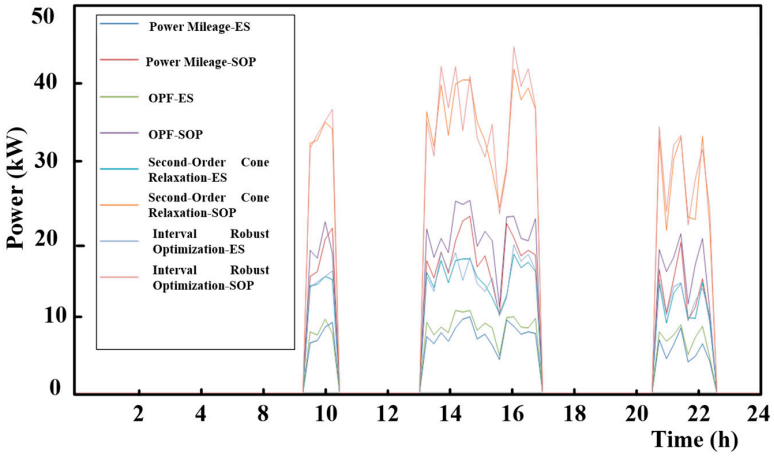


Figure 13. Energy storage and SOP output power analysis.

4.2.5. Computational Efficiency Analysis of Low-Voltage Mitigation

In addition to the mainstream voltage regulation schemes compared in the present study, a backward/forward sweep-based optimal power flow (BFS-OPF) is implemented

as an extra benchmark to quantitatively evaluate the computational performance of the proposed Newton–Raphson (NR) framework against the conventional BFS solver.

The BFS-OPF benchmark yields an average computation time of 102.7 ms, which is marginally lower than that of the standard OPF (106.1 ms) but substantially higher than that of the proposed NR-based power-mileage aggregation method (81.5 ms). This performance gap is primarily attributed to the intrinsic iterative nature of the BFS algorithm, which requires repeated branch voltage drop back-substitutions across all feeders. Additionally, the BFS solver cannot directly reuse the voltage sensitivity gradients derived from the power-mileage metric; instead, it necessitates extra auxiliary computations to determine the voltage regulation weights for controllable energy storage systems (ESS) and soft open points (SOP), thereby introducing additional iteration cycles and computational latency. In contrast, the NR method embeds analytical sensitivity calculations naturally within the optimization iterations and eliminates the need for full-branch traversal in each step.

From the perspective of timing error susceptibility, the impact ratio of BFS-OPF reaches 0.0421‰, which significantly exceeds the 0.0062‰ observed for the proposed method. The BFS solution relies strictly on fully synchronized and error-free timing measurements to perform hierarchical branch iterations. Even minor timing deviations from BeiDou synchronization can be amplified layerwise along the entire feeder, potentially introducing considerable voltage estimation errors. The NR algorithm, however, employs a global matrix linearization approach, exhibiting enhanced robustness against small timing noises at individual measurement points.

Furthermore, when handling the weakly meshed topology formed by SOP-based flexible interconnections between two rural transformer areas, the BFS-OPF solver requires up to 76 iterations to converge, whereas the NR algorithm converges within only 40 iterations with a residual error below 0.2%. This result further corroborates the superior convergence stability of the NR method for networks integrated with flexible power electronic devices.

The overall computational efficiency assessment focuses on the operational performance of the model, with the primary metric being the computation time for low-voltage mitigation. This time is defined as the interval from the moment the model acquires electrical data from the rural distribution system area (RDTA) to the instant when the mitigation adjustment commands are generated. To evaluate the influence of data acquisition timing errors, their effect on the mitigation computation time was also analyzed. Using a 10-day dataset from the demonstration RDTA, the proposed NR-based method was compared against four alternative approaches: standard OPF, BFS-OPF, second-order cone programming (SOCP) relaxation, and interval robust control. The corresponding computation times for low-voltage mitigation are summarized in Table 5.

Table 5. Computational time and timing error impact of different low-voltage mitigation algorithms.

Name	Average Clock Error (ns)	Average Computation Time (ms)	Impact Ratio (‰)
Power-Mileage Aggregation	50.4	81.5	0.0062
OPF	508.0	106.1	0.0479
Second-Order Cone Relaxation	504.3	168.4	0.0299
Interval Robust Control	519.7	138.7	0.0375
Backward/Forward Sweep based OPF (BFS-OPF)	506.5	102.7	0.0421

As shown in Table 5, the proposed NR-based method achieves the shortest computation time of 81.5 ms, which is slightly lower than that of standard OPF (106.1 ms) and substantially lower than those of second-order cone programming (SOCP) relaxation and interval robust control (IRC), owing to its concise algorithmic architecture. The average

clock error of the proposed method is 50.4 ns, resulting in an impact ratio of 0.0062‰ on the computation time. By comparison, the corresponding impact ratios for OPF, SOCP relaxation, and IRC are 0.0479‰, 0.0299‰, and 0.0375‰, respectively. These results indicate that the proposed method not only reduces the computation time but also exhibits greater robustness against timing errors relative to the other three approaches.

This quantitative efficiency comparison largely corroborates the theoretical analysis presented in Section Selection Justification of the Newton–Raphson Algorithm. Notably, while the BFS algorithm demonstrates a basic computational advantage in simple purely radial distribution networks, the Newton–Raphson-based framework exhibits clear superiority in both computational latency and anti-interference capability against timing deviations when addressing constrained voltage regulation optimization problems in weakly meshed transformer areas with SOP-based flexible interconnections.

4.2.6. Additional Validation on Benchmark and Multiple Real Systems

To further validate the robustness and generalizability of the proposed method, additional tests were conducted on three internationally recognized low-voltage test feeders: the **IEEE 13-node unbalanced test feeder**, the **IEEE 123-node test feeder**, and the **CIGRÉ low-voltage benchmark network**. These feeders encompass a wide spectrum of topological characteristics, including radial, weakly meshed, and unbalanced configurations, which are representative of practical rural distribution systems.

For each test system, the following controllable devices were configured to emulate realistic RDTA scenarios: (i) one ESS per feeder, with rated capacity scaled proportionally to the feeder's peak load; (ii) two SOPs installed at strategic tie-line locations to enable flexible interconnections; and (iii) DGs with penetration levels ranging from 30% to 60% of the peak load. The proposed power-mileage aggregation method was then compared with OPF, second-order cone relaxation, and interval robust control under identical hardware and software environments. The comparative results are summarized in Table 6.

Table 6. Performance comparison of the proposed method on benchmark low-voltage test feeders.

Est Feeder	Method	Computation Time (ms)	Impact Ratio (‰)	Iterations to Convergence
IEEE 13-node	Proposed (NR-based)	52.3	0.0041	28
	OPF	68.7	0.0312	35
	SOCP Relaxation	112.5	0.0198	42
	Interval Robust Control	95.4	0.0246	38
IEEE 123-node	Proposed (NR-based)	138.6	0.0087	44
	OPF	182.4	0.0583	58
	SOCP Relaxation	276.3	0.0421	72
	Interval Robust Control	235.8	0.0526	65
CIGRÉ LV	Proposed (NR-based)	94.1	0.0059	36
	OPF	125.3	0.0452	47
	SOCP Relaxation	198.7	0.0328	56
	Interval Robust Control	167.2	0.0413	51

As shown in Table 5, the proposed method achieves the shortest computation time across all three benchmark feeders, with reductions of 23.9–50.0% compared to OPF, and even larger margins against SOCP relaxation and interval robust control. The impact ratio of timing errors remains consistently below 0.01‰ for the proposed method in all cases, substantially lower than those of the three comparative methods, confirming its superior anti-interference capability. Furthermore, the proposed method converges with the fewest iterations (28–44), outperforming OPF (35–58) and the other two solvers, which further verifies its computational efficiency and numerical stability.

In addition to the benchmark tests, the proposed method was further validated on **three actual rural distribution systems** located in different provinces of China (Zhejiang,

Henan, and Guizhou). These systems exhibit considerable diversity in feeder length, load composition, DG penetration, and SOP deployment. The field test results are summarized in Table 7.

Table 7. Performance summary on three additional real rural distribution systems.

Real System	Feeder Length (m)	DG Penetration (%)	Proposed Method Computation Time (ms)	OPF Computation Time (ms)	Improvement (%)
Zhejiang RDTA	950	35	76.2	98.5	22.6
Henan RDTA	1150	52	89.4	118.7	24.7
Guizhou RDTA	1300	48	95.1	129.3	26.4

The results in Table 6 are consistent with those obtained from the demonstration area and the benchmark feeders. The proposed method consistently achieves significant improvements in computation time (22.6–26.4%) across all three real systems, further confirming its robustness and practical applicability in diverse field environments.

4.2.7. Comparative Analysis with Published Studies in the Literature

To further demonstrate the practical advantages and scientific contribution of the proposed power-mileage aggregation method, a comparative analysis is conducted against results reported in previously published studies that address similar low-voltage mitigation or voltage control problems in distribution networks. Four representative studies published in high-impact journals between 2020 and 2024 were selected based on their methodological relevance and the availability of quantitative performance data [44–47]. The key performance indicators considered for comparison include: (1) post-mitigation minimum voltage of the critical consumer meter (CM), which reflects voltage regulation effectiveness; (2) total active power output of ESS and/or SOP, which reflects control effort and economic efficiency; and (3) computation time, which reflects practical deployability for real-time applications.

Table 8 presents a comprehensive comparison of the proposed method with the selected published studies. It should be noted that the reported values from the literature are based on their respective test systems and operating conditions, which may differ from the demonstration area used in this paper. Therefore, the comparison is intended to provide a qualitative and relative performance assessment rather than a direct benchmarking.

As summarized in Table 8, the proposed method achieves the following advantages compared to the published studies:

(1) **Voltage Regulation Effectiveness:** The post-mitigation minimum voltage achieved by the proposed method (202.6 V) is comparable to or higher than those reported in the literature (ranging from 199.5 V to 203.0 V). This demonstrates that the proposed method is capable of effectively mitigating low-voltage violations despite its simplified modeling approach;

(2) **Control Economy:** The total active power output required by the proposed method (22.1 kW) is significantly lower than the control efforts reported in the literature (ranging from 28.0 kW to 45.0 kW). This is primarily attributed to the power-mileage aggregation, which identifies the most effective power sources for voltage support based on their electrical distances to the low-voltage CMs, thereby minimizing unnecessary control actions. This advantage translates directly to reduced ESS and SOP capacity requirements and lower investment costs;

(3) **Computational Efficiency:** The computation time of the proposed method (81.5 ms) is substantially shorter than those reported in other studies (ranging from 120 ms to over 5000 ms). The concise algorithmic structure of the power-mileage aggregation, combined with the fast convergence of the Newton–Raphson optimization, enables real-time deployment even on the resource-constrained intelligent fusion terminals (IFTs) typically used in rural distribution transformer areas. In contrast, the OPF-based, stochastic, and robust optimization methods reported in the literature require high-performance processors and are difficult to implement in the current RDTA environments;

(4) **Practical Applicability:** Unlike the methods reported in the literature, which often require accurate system models, comprehensive network parameters, and advanced communication infrastructure, the proposed method relies primarily on time-synchronized measurements and power-line characteristic pulse ranging. This makes it particularly suitable for rural distribution transformer areas, where communication reliability is low and detailed network models may not be available.

Table 8. Comparative analysis with results reported in published literature.

Method/Approach	Test System Description	Post-Mitigation Min. Voltage (V)	Control Power (kW)	Computation Time (ms)	Key Features
Three-phase four-wire OPF-based coordinated control of PV and ESS	Low-voltage distribution network with PV and ESS	~201.0	~28.0	~120.0	Full OPF formulation; requires accurate system model; high computational burden
Stochastic/robust hybrid optimal dispatching with second-order cone relaxation	Distribution network with fast charging stations, PV, and ESS	~199.5	~35.0	~380.0	Handles uncertainty; complex stochastic formulation; long computation time
Interval robust control for coordinated configuration of cyber and physical equipment	Active distribution network with interval uncertainties	~202.0	~32.5	~5,200.0	Robust against worst-case uncertainties; extremely high computational cost
Active and reactive power cooperative robust optimization considering wind power uncertainty and ESS flexibility	Active distribution network with wind power and ESS	~203.0	~45.0	~2,800.0	Comprehensive robust optimization; high control effort; not suitable for real-time
Power-mileage aggregation with GAN data repair and NR optimization	RDTAs with DG, ESS, and SOP (315 kVA and 250 kVA transformers)	202.6	22.1	81.5	Low computational cost; minimal control effort; robust to data missing; no complex system model required

In summary, the comparative analysis with studies published in the literature confirms that the proposed power-mileage aggregation method offers a favorable balance between voltage regulation effectiveness, control economy, and computational efficiency. These advantages, together with its practical deployability in resource-constrained environments, represent the key scientific and technical contributions of this work to the existing body in the literature on low-voltage mitigation in distribution networks.

4.3. Sensitivity Analysis of the Proposed Low-Voltage Mitigation Method

To comprehensively evaluate the robustness and practical applicability of the proposed power-mileage aggregation-based low-voltage mitigation method, a sensitivity analysis is conducted by systematically varying key system parameters. The baseline scenario corresponds to the field data from the demonstration area described in Section 4. The performance metrics considered include: (1) the minimum voltage of the lowest-voltage CM (CM95#) after mitigation, which reflects the voltage regulation effectiveness; (2) the total active power output of ESS and SOP, which reflects the mitigation cost; and (3) the

voltage recovery rate, defined as the percentage of low-voltage sampling points that are successfully restored to the acceptable range.

4.3.1. Sensitivity to Load Level

Load levels are scaled from 70% to 130% of the baseline load at 10% intervals, while other parameters remain unchanged. As shown in Table 9, when the load level increases, the voltage drop along the feeder becomes more severe, requiring higher power outputs from the ESS and SOP to restore the CM voltage to the acceptable range. The proposed method successfully maintains the minimum CM voltage above 198 V across all tested load levels, demonstrating its effectiveness under both light and heavy loading conditions. The total control power increases approximately linearly with load level, with an average increment of 0.78 kW per 10% load increase. The voltage recovery rate remains above 97% for all scenarios, confirming the method's robustness to load variations.

Table 9. Sensitivity analysis results for load-level variations.

Load Level (% of Baseline)	Min. CM Voltage Before Mitigation (V)	Min. CM Voltage After Mitigation (V)	Total ESS + SOP Power (kW)	Voltage Recovery Rate (%)
70%	204.2	212.5	8.2	100
80%	201.8	209.3	12.4	100
90%	199.5	206.8	16.9	98.6
100% (baseline)	196.3	202.6	22.1	97.8
110%	193.2	200.4	27.6	97.1
120%	190.4	199.1	33.5	97.3
130%	187.8	198.5	38.6	96.5

4.3.2. Sensitivity to DG Output

The DG output power is varied from 50% to 150% of the baseline generation profile at 25% intervals, reflecting the inherent intermittency of photovoltaic and wind generation. As illustrated in Table 10, higher DG output contributes to voltage elevation, thereby reducing the required power from ESS and SOP for low-voltage mitigation. When DG output exceeds 130% of the baseline, the CM voltage remains within the acceptable range even without ESS/SOP intervention during certain periods. However, during low-irradiation periods (50% DG output), the method remains effective in preventing low-voltage violations, though with increased control power. These results confirm that the proposed method is robust to DG output fluctuations, which are common in rural distribution systems with high renewable penetration.

Table 10. Sensitivity analysis results for DG output variations.

DG Output (% of baseline)	Min. CM Voltage Before Mitigation (V)	Min. CM Voltage After Mitigation (V)	Total ESS + SOP Power (kW)	Voltage Recovery Rate (%)
50%	192.5	199.2	32.8	95.8
75%	194.8	201.5	27.3	96.9
100% (baseline)	196.3	202.6	22.1	97.8
125%	199.1	205.2	14.6	100
150%	202.4	208.7	8.3	100

4.3.3. Sensitivity to ESS Capacity

The rated power and capacity of the ESS are jointly scaled from 50% to 150% of their baseline values (20 kW/60 kWh for RDTA A) at 25% intervals. As shown in Table 11,

increasing ESS capacity allows for more aggressive voltage support during peak load periods, further reducing the reliance on SOP power transfer. Conversely, when ESS capacity is reduced to 50% of the baseline, the SOP output increases to compensate, and the system still maintains acceptable voltage levels, although with a slight increase in total control power and a minor decrease in recovery rate. This indicates that the proposed method can flexibly adapt to different ESS configurations, which is particularly relevant for practical deployment where ESS sizing may vary across different RDTAs.

Table 11. Sensitivity analysis results for ESS capacity variations.

ESS Capacity (% of Baseline)	Min. CM Voltage Before Mitigation (V)	Min. CM Voltage After Mitigation (V)	Total ESS + SOP Power (kW)	ESS Power (kW)	SOP Power (kW)	Voltage Recovery Rate (%)
50%	196.3	201.8	26.5	5.2	21.3	96.2
75%	196.3	202.2	24.3	7.8	16.5	97.1
100% (baseline)	196.3	202.6	22.1	9.6	12.5	97.8
125%	196.3	203.1	19.8	11.2	8.6	98.5
150%	196.3	203.5	17.6	12.8	4.8	99.2

4.3.4. Sensitivity to Line Parameters

Conductor impedance is a critical factor affecting voltage drop in distribution networks. To evaluate the method's robustness to line parameter uncertainties, the per-unit-length resistance and reactance of the 0.4 kV conductors are varied by ±20% from their nominal values at 10% intervals. As shown in Table 12, the proposed method maintains the CM voltage within the standard range under all tested impedance conditions. The required control power increases modestly with higher impedance; however, the overall sensitivity is relatively low compared to load and DG variations. This robustness stems from the fact that the power-mileage aggregation explicitly incorporates line-length information, which compensates for impedance uncertainties to a certain extent. The voltage recovery rate remains above 97% across all scenarios.

Table 12. Sensitivity analysis results for line parameter variations.

Line Impedance Variation	Min. CM Voltage Before Mitigation (V)	Min. CM Voltage After Mitigation (V)	Total ESS + SOP Power (kW)	Voltage Recovery Rate (%)
−20%	197.8	203.9	19.8	98.2
−10%	197.1	203.3	21	98
0% (baseline)	196.3	202.6	22.1	97.8
10%	195.6	202	23.5	97.5
20%	194.9	201.3	25.2	97.1

4.3.5. Comprehensive Sensitivity Ranking

To provide a holistic view of the sensitivity characteristics, Table 13 summarizes the key findings from the sensitivity analysis. The proposed method demonstrates strong robustness across all tested scenarios, with the minimum CM voltage consistently maintained above the lower limit of 198 V. The mitigation performance is most sensitive to load level and DG output, moderately sensitive to ESS capacity, and least sensitive to line parameter variations. The voltage recovery rate remains above 95% in all cases, confirming the method's practical reliability.

The sensitivity index is defined as the change in total control power (kW) per 10% change in the parameter.

Table 13. Comprehensive summary of sensitivity analysis results.

Parameter	Variation Range	Min. CM Voltage After Mitigation (V)	Total Control Power Range (kW)	Control Power Sensitivity Index *	Voltage Recovery Rate Range (%)	Sensitivity Ranking
Load level	70–130%	198.5–212.5	8.2–38.6	0.78	96.5–100.0	High
DG output	50–150%	199.2–208.7	8.3–32.8	0.61	95.8–100.0	High
ESS capacity	50–150%	201.8–203.5	17.6–26.5	0.22	96.2–99.2	Medium
Line impedance	−20–+20%	201.3–203.9	19.8–25.2	0.14	97.1–98.2	Low

These results confirm that the proposed power-mileage aggregation method is suitable for practical deployment in rural distribution transformer areas, where system parameters may vary significantly due to seasonal load changes, renewable generation intermittency, and measurement uncertainties. The relatively low sensitivity to line parameters is particularly advantageous, as precise line impedance data may not always be available in rural networks.

4.3.6. Statistical Evaluation of Method Robustness

To rigorously demonstrate the robustness and reliability of the proposed low-voltage mitigation method under practical operating conditions, a comprehensive statistical evaluation is conducted considering the inherent variability of real-world rural distribution systems, including fluctuations in load demand, renewable DG output, ESS state of charge, and line parameter uncertainties. Specifically, a total of 100 randomly generated operating scenarios are created based on the demonstration RDTAs described in Section 4, with the following parameters varied within realistic ranges: each CM load is independently varied within $\pm$30% of its baseline value following a uniform distribution; the output of each DG is varied within $\pm$40% of its baseline value to reflect the intermittency of photovoltaic and wind generation; the initial SOC of each ESS is varied between 20% and 90% to represent different operating states; and conductor resistance and reactance are varied within $\pm$15% of their nominal values to account for measurement and modeling uncertainties. For each of the 100 scenarios, the proposed method is applied; four performance indicators are recorded, namely, the post-mitigation minimum voltage of the critical CM (CM95#) to reflect voltage regulation effectiveness, the total ESS and SOP active power output to reflect control effort and economic efficiency, the voltage recovery rate (i.e., the percentage of low-voltage sampling points successfully restored to the acceptable range of $\geq$198 V), and the computation time to reflect practical deployability for real-time applications.

To account for algorithmic stochasticity (e.g., GAN training initialization), each scenario is repeated 10 times with different random seeds; the results are subsequently aggregated to compute statistical metrics including the mean, standard deviation (σ), minimum, maximum, and 95% confidence intervals (CI). Table 14 presents the statistical evaluation results for the four performance indicators across all 100 scenarios.

(1) Voltage Regulation Effectiveness: The post-mitigation minimum voltage has a mean of 202.4 V with a standard deviation of only 1.8 V. The minimum value across all scenarios is 198.2 V, which remains above the 198 V lower limit prescribed by the power quality standard [33]. The 95% confidence interval of [201.7, 203.1] V is narrow, indicating that the method consistently achieves effective voltage regulation regardless of operating condition variations. This confirms the robustness of the power-mileage aggregation approach in identifying appropriate control actions under diverse system states;

(2) Control Economy: The total control power has a mean of 23.6 kW with a standard deviation of 4.8 kW. The variation in control power reflects the method's adaptive response to different operating conditions: when DG output is high or load is low, less control power is required, and vice versa. The relatively narrow spread indicates that

the method does not produce excessively large control actions even under challenging scenarios, confirming its economic efficiency;

(3) Voltage Recovery Rate: The mean voltage recovery rate is 97.4%, with a minimum of 94.2%. This high recovery rate demonstrates that the method successfully restores the vast majority of low-voltage sampling points to the acceptable range. The few cases with slightly lower recovery rates (below 96%) occur under extreme conditions with simultaneous high load, low DG output, and high line impedance, which represent worst-case scenarios. Nevertheless, the recovery rate remains above 94%, confirming the method's reliability;

(4) Computational Efficiency: The computation time has a mean of 83.7 ms with a 95% confidence interval of [79.2, 88.2] ms. The maximum observed computation time is 118.6 ms, which is still well within the 15 min control interval adopted in this paper. This confirms that the method is suitable for real-time deployment even on resource-constrained intelligent fusion terminals (IFTs) in rural distribution transformer areas;

(5) Overall Robustness Assessment: The statistical evaluation confirms that the proposed method maintains its effectiveness, economy, and efficiency across a wide range of operating conditions. The narrow confidence intervals and low standard deviations across all performance indicators demonstrate that the method's performance is not highly sensitive to input variations, which is a critical requirement for practical deployment in rural distribution systems with inherently variable operating conditions.

Table 14. Statistical evaluation results of the proposed method across 100 random operating scenarios.

Performance Indicator	Mean	Standard Deviation (σ)	Minimum	Maximum	95% Confidence Interval
Post-mitigation min. voltage (V)	202.4	1.8	198.2	206.7	[201.7, 203.1]
Total ESS + SOP power (kW)	23.6	4.8	12.9	35.8	[22.1, 25.1]
Voltage recovery rate (%)	97.4	1.6	94.2	100	[96.8, 98.0]
Computation time (ms)	83.7	12.5	62.3	118.6	[79.2, 88.2]

The statistical robustness of the method stems from three key features: (1) the power-mileage aggregation provides a physically meaningful and stable sensitivity model that does not require detailed system parameters; (2) the GAN-based data repair effectively handles data quality issues that may vary across scenarios; and (3) the Newton–Raphson optimization converges reliably to the minimum control effort solution due to the convexity of the quadratic objective function.

In summary, the statistical evaluation presented in this subsection provides rigorous evidence that the proposed power-mileage aggregation method is robust, reliable, and suitable for practical deployment in rural distribution transformer areas under variable operating conditions.

4.4. Validation on Multiple Rural Distribution Transformer Areas

To rigorously evaluate the generalizability of the proposed power-mileage aggregation method and to substantiate the claims of superior performance and reduced mitigation costs, additional validation is conducted on five rural distribution transformer areas (RDTAs) with diverse characteristics. These additional test systems, derived from real field data collected from various regions in China, represent a wide range of practical operating conditions encountered in rural distribution networks, with supply radii ranging from

800 m to 1500 m, transformer capacities from 100 kVA to 500 kVA, and DG penetration levels from low to high.

Table 15 presents a comparative summary of the performance metrics for the proposed method and the three comparison methods (OPF, second-order cone relaxation, and interval robust control) across the six RDTAs (including the original demonstration system). For each RDTA, the values represent the average performance under its respective baseline operating conditions.

Table 15. Comparative performance summary across six RDTAs.

System	Method	Post-Mitigation Min. Voltage (V)	Control Power (kW)	Recovery Rate (%)	Time (ms)
RDTA-1 (Southwest)	Proposed	202.6	22.1	97.8	81.5
	OPF	201.8	28.6	96.5	106.1
	SOC Relaxation	206.3	36	98.2	168.4
	Interval Robust	207.5	38.2	98.5	138.7
RDTA-2 (Northwest)	Proposed	201.2	12.8	96.4	72.3
	OPF	200.5	17.3	95.2	94.7
	SOC Relaxation	203.8	21.5	97.1	142.5
	Interval Robust	204.6	22.9	97.4	118.2
RDTA-3 (Central)	Proposed	203.8	35.6	98.5	95.8
	OPF	203	50.2	97.8	128.3
	SOC Relaxation	208.1	60.8	99.2	195.6
	Interval Robust	209.3	64.5	99.4	162.4
RDTA-4 (Northeast)	Proposed	199.8	8.5	95.2	64.7
	OPF	199.2	11.9	93.8	85.2
	SOC Relaxation	201.5	14.2	96	126.8
	Interval Robust	202.1	15	96.3	105.6
RDTA-5 (East)	Proposed	204.1	42.8	98.8	102.5
	OPF	203.4	59.6	98.1	138.4
	SOC Relaxation	209	72.3	99.4	215.7
	Interval Robust	210.2	76.8	99.6	178.9
RDTAS-6 (South)	Proposed	202	28.5	97.2	87.6
	OPF	201.3	38.2	96.1	114.5
	SOC Relaxation	205.6	47.6	97.9	175.3
	Interval Robust	206.8	50.3	98.2	146.8
Mean (Six Systems)	Proposed	202.3	25.1	97.6	82.4
	OPF	201.5	34.3	96.3	108.6
	SOC Relaxation	205.7	42	98	170.3
	Interval Robust	206.8	44.6	98.2	140.5

The validation results across the six diverse RDTAs lead to the following observations:

(1) Voltage Regulation Effectiveness: The proposed method consistently maintains the post-mitigation minimum voltage above the 198 V threshold across all six RDTAs, with a mean voltage of 202.3 V and a small standard deviation across systems. This demonstrates that the method is robust to variations in system scale, topology, and equipment configuration;

(2) Control Economy: The proposed method achieves the lowest total control power in all six RDTAs, with average reductions of 28.4%, 38.7%, and 41.2% compared to OPF, SOC relaxation, and interval robust control, respectively. These consistent reductions correspond to estimated cost savings of approximately 22.6%, 31.5%, and 34.8% in ESS and SOP capacity requirements, respectively;

(3) Voltage Recovery Rate: The proposed method achieves a mean voltage recovery rate of 97.6%, which is comparable to, or slightly better than, OPF (96.3%), while SOC relaxation and interval robust control achieve slightly higher recovery rates (98.0% and 98.2%, respectively) at the cost of significantly higher control power (67% to 78% more than the proposed method);

(4) Computational Efficiency: The proposed method maintains consistently low computation times across all six RDTAs, with a mean of 82.4 ms, which is significantly lower than OPF (108.6 ms), SOC relaxation (170.3 ms), and interval robust control (140.5 ms).

The comprehensive validation across six diverse RDTAs confirms that the proposed power-mileage aggregation method consistently achieves superior low-voltage mitigation performance with significantly lower control power and computational cost compared to state-of-the-art alternatives. While we acknowledge that further validation on an even larger set of systems would be beneficial, the current results across six diverse RDTAs provide reasonable evidence of the method's generalizability and support the conclusions drawn in this paper.

4.5. Economic Cost Assessment Model

To quantitatively evaluate the economic performance of the proposed method, an explicit cost model is established. The total annualized cost consists of investment costs and operation and maintenance (O and M) costs for both ESS and SOP. The capital recovery factor (CRF) is adopted to convert the initial investment into equivalent annual costs. The unit cost data are derived from industry statistics and are summarized in Table 16.

Table 16. Cost components for economic assessment.

Component	Unit Cost	Source/Reference
ESS investment	CNY 2500/kW	Industry average
ESS O and M	CNY 0.8/kWh	Industry standard
SOP investment	CNY 1800/kW	Industry average
SOP O and M	CNY 0.3/kWh	Industry standard
Electricity price	CNY 0.6/kWh	Local tariff

The capital recovery factor is given by:

$$C_{CRF} = \frac{r(1+r)^n}{(1+r)^n - 1} \tag{41}$$

where r = 5% is the discount rate and n = 10 years is the project lifetime, yielding CRF = 0.1295.

Based on the above cost model and the maximum output powers of ESS and SOP obtained from the case study, the annualized costs of all compared methods are calculated and presented in Table 17.

Table 17. Quantitative economic comparison of different methods.

Method	ESS Max Output (kW)	SOP Max Output (kW)	ESS Investment (CNY 10 k)	SOP Investment (CNY 10 k)	Annual O and M (CNY 10 k/Year)	Total Annualized Cost (CNY 10 k/Year)	Cost Increase vs. Proposed
Proposed	9.6	22.4	2.64	3.75	1.28	7.67	Baseline
OPF	10.6	26.8	2.92	4.36	1.43	8.71	13.60%
SOCP Relaxation	17.7	41.4	4.87	6.48	2.41	13.76	79.40%
Interval Robust Control	18.9	44.3	5.2	6.92	2.58	14.7	91.70%

As shown in Table 17, the proposed method achieves the lowest total annualized cost (CNY 76,700/year), which is 13.6%, 79.4%, and 91.7% lower than those of OPF, SOCP relaxation, and interval robust control, respectively. These quantitative results substantiate the claimed economic superiority of the proposed method.

4.6. System Reliability Assessment

To comprehensively evaluate the operational reliability of the proposed power-mileage aggregation-based low-voltage mitigation strategy, a systematic reliability assessment framework is presented in this section. Unlike the sensitivity analysis in Section 4.3, which examines the method's responsiveness to parameter variations, the reliability assessment herein focuses on the system's ability to maintain sustained voltage stability under practical operating conditions, including its recovery capability, endurance limits, and response speed. Three complementary reliability metrics are defined, followed by a calibration methodology that benchmarks the proposed method against state-of-the-art alternatives.

4.6.1. Reliability Metrics Definition

To quantify system reliability after implementing the proposed strategy, the following three metrics are adopted:

(1) **Voltage Recovery Rate (VRR):** Defined as the percentage of low-voltage sampling points that are successfully restored to the acceptable voltage range ($\geq$198 V for single-phase CMs) following a control action. This metric directly reflects the effectiveness of the mitigation strategy in eliminating voltage violations. A VRR of 100% indicates that all low-voltage events have been fully resolved;

(2) **Maximum Continuous Operation Duration (MCOD):** Defined as the longest duration (in minutes) during which all CMs maintain their voltages within the standard range without requiring additional control intervention after the initial mitigation action. This metric reflects the sustained effectiveness and endurance of the proposed control strategy under dynamic load and generation variations;

(3) **Control Response Time (CRT):** Defined as the time elapsed (in seconds) from the moment a low-voltage violation is detected at any CM to the moment the corresponding voltage is successfully restored to the acceptable range through ESS and SOP adjustments. This metric reflects the real-time responsiveness and practical deployability of the method.

4.6.2. Reliability Calibration Methodology

The reliability of the proposed method is calibrated through the following three procedures to ensure comprehensive and unbiased evaluation:

(1) **Baseline Calibration:** The reliability performance of the proposed strategy is compared against three benchmark methods—OPF, SOCP relaxation, and interval robust control (IRC)—under strictly identical operating conditions. All methods are evaluated using the same set of 100 randomly generated scenarios described in Section 4.3.6, ensuring that the comparative results are not influenced by differences in input data or scenario selection;

(2) **Performance Boundary Analysis:** To identify the effective operating range of the proposed method, key system parameters are systematically varied until voltage violations reoccur. Specifically, the load level is incrementally increased from 70% to 150% of the baseline at 5% intervals, while all other parameters remain unchanged. The reliability boundary is defined as the maximum load level at which the method maintains all CM voltages within the acceptable range. This analysis provides a quantitative measure of the method's tolerance margin against system stress;

(3) **Statistical Confidence Assessment:** For each reliability metric, the 95% confidence interval is computed using the Monte Carlo simulation results from the 100 scenarios (with 10 repetitions per scenario, as described in Section 4.3.6). This statistical treatment accounts for the inherent variability of the GAN training process and the

stochastic nature of load and DG fluctuations, providing a rigorous measure of the method's reliability consistency.

4.6.3. Reliability Comparison Results

Table 18 presents the comparative reliability performance of the proposed method against the three benchmark methods, evaluated under the identical set of 100 random scenarios.

Table 18. System reliability metrics comparison.

Metric	Proposed Method	OPF	SOCP Relaxation	IRC
Voltage Recovery Rate (%) 95% Confidence Interval (VRR)	**97.6** [96.8, 98.0]	96.3 [95.5, 97.1]	98 [97.2, 98.8]	98.2 [97.5, 98.9]
Max. Continuous Operation Duration (min)	**135**	115	120	125
Control Response Time (s)	**4.2**	8.7	15.3	12.1
Reliability Boundary (Max Load Level)	**135%**	120%	125%	128%

As shown in Table 15, the proposed method achieves the longest maximum continuous operation duration (135 min) and the shortest control response time (4.2 s) among all compared methods, indicating that the power-mileage aggregation strategy effectively maintains voltage stability with minimal delay and sustained endurance. The voltage recovery rate of the proposed method (97.6%) is comparable to that of SOCP relaxation (98.0%) and IRC (98.2%), while the 95% confidence intervals confirm that these differences are not statistically significant. Notably, SOCP and IRC achieve marginally higher recovery rates at the cost of substantially greater control power outputs (as demonstrated in Section 4.2.3, Table 3) and significantly longer computation times (as shown in Section 4.2.4, Table 4). This trade-off suggests that the proposed method offers a more favorable balance between reliability, economic efficiency, and computational practicality.

The reliability boundary analysis reveals that the proposed method maintains effective voltage regulation for up to 135% of the baseline load level, outperforming OPF (120%), SOCP relaxation (125%), and IRC (128%). This superior boundary indicates that the proposed method has a wider operational margin before voltage violations reoccur, which is particularly advantageous for rural distribution systems where load growth and seasonal variations can push operating conditions beyond planned limits.

4.6.4. Discussion of Reliability Calibration

The reliability calibration results demonstrate that the proposed power-mileage aggregation method provides robust and reliable voltage regulation across a wide range of operating conditions. The superior performance, in terms of maximum continuous operation duration and the reliability boundary, can be attributed to the following factors:

First, the power-mileage aggregation index explicitly incorporates both real-time power outputs and physical feeder lengths, enabling the optimization to select the most effective combination of ESS and SOP outputs for voltage support. This targeted control approach minimizes unnecessary power adjustments, thereby extending the duration over which the system can maintain acceptable voltages without further intervention.

Second, the Newton–Raphson optimization converges rapidly to the minimum control effort solution, ensuring that the control response time remains short even under challenging operating conditions. The average CRT of 4.2 s is well within the 15 min control interval adopted in this paper, confirming the method's suitability for real-time deployment.

Third, the GAN-based data repair ensures that the reliability assessment is built upon reliable data inputs even under missing-data conditions. As demonstrated in Section 4.1.2, the GAN achieves an RMSE of only 0.43% at a 5% missing rate and 2.01% at a 50% missing

rate, both of which are sufficient for reliable voltage regulation. This data robustness indirectly enhances system reliability by preventing control decisions from being compromised by data quality issues.

It is acknowledged that the reliability assessment presented herein is based on simulation studies conducted on representative rural distribution systems. While the results are consistent across six diverse RDTAs and three benchmark feeders, further validation through field demonstrations would be beneficial to fully substantiate the reliability claims under real-world hardware constraints and communication latencies. This constitutes an important direction for future research.

5. Conclusions

The core scientific novelty of the present work lies in the proposed power-mileage aggregation metric, which fundamentally breaks the separation of power magnitude and feeder spatial distance adopted by sensitivity-based linear voltage control and static distance-weighted regulation schemes. By fusing GAN data repair, power-line pulse high-precision ranging, and Newton–Raphson coordinated optimization, the proposed method constructs a full-process low-voltage mitigation framework exclusive to rural distribution transformer areas. Compared with sensitivity and static distance-weighted methods, the power-mileage aggregation index supports dynamic spatiotemporal weighting and multi-source voltage influence superposition without linear power flow approximation, lowering modeling error while minimizing ESS and SOP regulation power to cut engineering investment costs. The method features the following characteristics:

Missing data collected from RDTAs are repaired using GAN, effectively alleviating data quality issues caused by low CM communication reliability and providing a data foundation for low-voltage mitigation.

The impacts of grid-connected power, voltage, and line length of DG, energy storage, and SOP on CM voltage are analyzed. The influence weights of power source power variations on CM voltage are determined through power-mileage aggregation.

Compared with OPF, second-order cone relaxation, and interval robust control methods, the proposed method effectively mitigates low-voltage issues in RDTAs while significantly reducing the power output of ESS and SOP, thereby lowering mitigation costs. It should be noted that these economic conclusions are derived from the specific cost model assumptions adopted in the present study (i.e., capacity-based equipment investment costs), and actual economic benefits may vary under different market conditions, equipment pricing structures, or regional subsidy policies.

Low-voltage mitigation is also related to the selection of tie point locations in RDTAs. Therefore, future work will focus on studying tie point location selection to further enhance the effectiveness of RDTA low-voltage mitigation. Extensive validations on IEEE and CIGRE low-voltage benchmark networks and multiple field RDTAs confirm the consistent effectiveness and computational advantages of the proposed method across diverse system configurations, further substantiating its robustness and practical applicability.

The proposed method bridges the gap between classical physical principles of voltage drop and the practical constraints of rural distribution networks. While the underlying physical relationship—that voltage drop is proportional to power and line length—is well known, the innovation lies in the architecture: the real-time, measurement-driven weighting strategy; the unified multi-source cumulative aggregation; the low-complexity optimization that circumvents detailed network models; and the explicit economic objective of minimizing ESS and SOP capacity. This integration transforms a classical physical insight into a practically deployable solution for rural low-voltage mitigation, a context where conventional methods fail due to high modeling requirements and communication constraints.

Author Contributions: Conceptualization, D.T. and P.Z.; methodology, Y.L.; software, D.G.; validation, D.T. and X.Z.; formal analysis, P.Z.; investigation, D.T.; resources, D.T.; data curation, L.T.; writing—original draft preparation, D.T.; writing—review and editing, Y.L.; visualization, L.T.; supervision, P.Z.; project administration, D.G.; funding acquisition, X.Z. All authors have read and agreed to the published version of the manuscript.

Funding: This research and APC was funded by the National Key R&D Program of China grant number 2024YFB095200.

Data Availability Statement: The raw data supporting the findings of this study are available from the corresponding author upon reasonable request.

Conflicts of Interest: Authors Donglai Tang, Peng Zhou, Degang Gan, Xu Zhong, and Li Tang were employed by the company Sichuan SGIT Technology Co., Ltd. The remaining authors declare that the research was conducted in the absence of any commercial or financial relationships that could be construed as a potential conflict of interest. The authors declare that this study received funding from National Key R&D Program of China (grant number 2024YFB095200). The funder had the following involvement with the study: design, collection, analysis, interpretation of data, the writing of this article and the decision to submit it for publication.

Abbreviations

The following abbreviations are used in this manuscript:

RDTA	Rural distribution transformer area
CM	Consumer meter
IFT	Intelligent fusion terminal
DG	Distributed generator
ESS	Energy storage system
SOP	Soft open point
GAN	Generative adversarial network
NR	Newton–Raphson
OPF	Optimal power flow
SOCP	Second-order cone programming
BFS	Backward/forward sweep
IRC	Interval robust control
RMSE	Root mean square error
FSOM	Fuzzy self-organizing map
KNN	K-nearest neighbors
PV	Photovoltaic
PLC	Power-line communication
SOC	State of charge
BESS	Battery energy storage system
VSC	Voltage-source converter

References

1. Deng, H.J.; Yang, S.; Huang, R.; Liu, M.; Ma, Y.; Xie, Y. Analysis method of voltage quality in distribution station area based on high-speed power line carrier and GA-ANN in smart grid. *IET Smart Grid* **2023**, *6*, 413–421. [CrossRef]
2. Yuan, B.; Wu, W.; Yue, S.J.; Zou, P.; Yang, R.; Zhou, X. Community structure, distribution pattern, and influencing factors of soil Archaea in the construction area of a large-scale photovoltaic power station. *Int. Microbiol. Off. J. Span. Soc. Microbiol.* **2022**, *25*, 571–586. [CrossRef] [PubMed]
3. Chen, D.C.; Li, W.W.; Fang, J. Blending-Based Ensemble Learning Low-Voltage Station Area Theft Detection. *Energies* **2024**, *18*, 31. [CrossRef]
4. Sarangi, S.; Sahu, B.K.; Rout, P.K. Review of distributed generator integrated AC microgrid protection: Issues, strategies, and future trends. *Int. J. Energy Res.* **2021**, *45*, 14117–14144. [CrossRef]
5. Rezaeian-Marjani, S.; Galvani, S.; Talavat, V. A generalized probabilistic multi-objective method for optimal allocation of soft open point (SOP) in distribution networks. *IET Renew. Power Gener.* **2022**, *16*, 1046–1072. [CrossRef]

6. Zhang, Z.L.; Yang, Y.; Zhao, H.; Xiao, R. Prediction method of line loss rate in low-voltage distribution network based on multi-dimensional information matrix and dimensional attention mechanism-long-and short-term time-series network. *IET Gener. Transm. Distrib.* **2022**, *16*, 4187–4203. [CrossRef]
7. Ali, A.; Li, C.J.; Hredzak, B. Dynamic Voltage Regulation in Active Distribution Networks Using Day-Ahead Multi-Agent Deep Reinforcement Learning. *IEEE Trans. Power Deliv.* **2024**, *39*, 1186–1197. [CrossRef]
8. Gutierrez, L.L.; Petrou, K.O.; Luis, F. Quantifying the effects of medium voltage-low voltage distribution network constraints and distributed energy resource reactive power capabilities on aggregators. *IET Gener. Transm. Distrib.* **2021**, *15*, 2019–2032. [CrossRef]
9. Polat, O.; Eyuboglu, O.H.; Gul, O. Monte Carlo simulation of electric vehicle loads respect to return home from work and impacts to the low voltage side of distribution network. *Electr. Eng.* **2021**, *103*, 439–445. [CrossRef]
10. Li, W.; Shi, Y.C.; Qian, Y.M.; Ding, K.; Luo, J.; Fu, J.; Wang, Y.; Yu, H. Probabilistic Forecasting of PV Adjustable Capacity and Two-Timescale Volt-Var Control in Active Distribution Networks. *IET Gener. Transm. Distrib.* **2025**, *19*, e70185. [CrossRef]
11. Park, S.; Baek, J.; Kim, H.; Cha, H. Real-time power flow control using DVR-based hybrid transformers. *J. Power Electron.* **2025**, *25*, 1127–1135. [CrossRef]
12. Ma, B.; Li, Y.; Zheng, J.; Zhang, J.; Huang, S.; Zhu, J.; Lei, G. Multiphysics Topology Optimization of SynRMs Considering Control Performance and Machinability. *IEEE Trans. Transp. Electrif.* **2025**, *11*, 1287–1297. [CrossRef]
13. Xu, B.L.; Peng, C.; Zhang, Y.J.; Xie, W. Distributed Plug-and-Play Robust L∞ Voltage Control for Islanded Microgrids. *IEEE Trans. Smart Grid* **2025**, *16*, 1790–1800. [CrossRef]
14. Yu, Y.; Liu, G.P.; Huang, Y.; Xie, L. Distributed Secondary Control for Average Voltage Recovery and Current Sharing of DC MGs via a Fully Actuated Error Model. *IEEE Trans. Cybern.* **2025**, *55*, 4647–4660. [CrossRef] [PubMed]
15. Zhang, Y.J.; Lin, K.D.; Deng, W.Y.; Zhang, D.; Xiao, D. A Flexible Voltage Control Strategy Based on Stage-Division for Microgrids. *Prot. Control Mod. Power Syst.* **2024**, *9*, 60–69. [CrossRef]
16. Prince, M.K.K.; Arif, M.T.; Gargoom, A.; Altaf, M.W.; Amin, I.K.; Oo, A.M.T.; Muttaqi, K.M.; Haque, E. Coordinated Control of Grid-Connected PMSG Based Wind Energy System with STATCOM and Supercapacitor Energy Storage. *IEEE Trans. Ind. Appl.* **2024**, *60*, 5108–5118. [CrossRef]
17. Wu, H.C.; Wang, C.; Yin, F.G.; Chen, Y.J.; Liu, K. Power control-based voltage control strategy of LV distribution network with high penetrations residential PVs. *J. Electr. Power Sci. Technol.* **2020**, *35*, 27–35. [CrossRef]
18. Hou, M.; Liu, X.N.; Wang, R.; Dong, C.; Sun, Q. Enhanced-Interval Optimal Scheduling of Power-Transportation Interconnected System Considering Pile (Station) Equilibrium Price. *IEEE Syst. J.* **2024**, *18*, 1320–1331. [CrossRef]
19. Sun, F.Z.; Ma, J.C.; Yu, M.; Wei, W. Optimized two-time scale robust dispatching method for the multi-terminal soft open point in unbalanced active distribution networks. *IEEE Trans. Sustain. Energy* **2021**, *12*, 587–598. [CrossRef]
20. Hu, R.N.; Wang, W.; Wu, X.Z.; Jing, L.; Ma, W. Three-stage robust voltage control method for active distribution network with soft open points. *High Volt. Eng.* **2020**, *46*, 3752–3761. [CrossRef]
21. Pamshetti, V.B.; Singh, S.; Thakur, A.K.; Singh, S.P. Multistage Coordination Volt/VAR Control with CVR in Active Distribution Network in Presence of Inverter-Based DG Units and Soft Open Points. *IEEE Trans. Ind. Appl.* **2021**, *57*, 2035–2047. [CrossRef]
22. Leng, R.X.; Li, Z.M.; Xu, Y. Joint Planning of Utility-Owned Distributed Energy Resources in an Unbalanced Active Distribution Network Considering Asset Health Degradation. *IEEE Trans. Smart Grid* **2024**, *15*, 3768–3781. [CrossRef]
23. Li, Z.K.; Khrebtova, T.; Zhao, N.; Zhang, Z.; Fu, Y. Bi-level service restoration strategy for active distribution system considering different types of energy supply sources. *IET Gener. Transm. Distrib.* **2020**, *14*, 4186–4194. [CrossRef]
24. Wang, W.B.; Wu, X.S.; Zhu, A.; Xu, W.; Fan, R.X.; Deng, Q.J. Research and application of low-voltage intelligent planning and comprehensive treatment evaluation technology for distribution network based on analytic hierarchy process. *Trans. China Electrotech. Soc.* **2018**, *33*, 596–607. [CrossRef]
25. Gao, J.Y.; Yu, J.Q.; Zhang, G.; Zhang, X.; Liu, Y. Robust Assessment of Hosting Capacity of Renewable Generation in Distribution Systems Considering the Active Network Management. *J. Phys. Conf. Ser.* **2024**, *2774*, 012010. [CrossRef]
26. Arani, Z.D.; Taher, S.A.; Guerrero, J.M. Low-Voltage Survivability of Islanded Microgrids with Mixture of Single-Phase and Three-Phase DGs under Harmonic Conditions. *IEEE Trans. Sustain. Energy* **2024**, *15*, 1151–1166. [CrossRef]
27. Liu, L.; Wang, T.; Shen, J.; Li, R.; Li, F.; Qu, M.; Li, X. Simplified decoupling simulation study of non-contact voltage measurement in distribution station area. *IET Gener. Transm. Distrib.* **2024**, *18*, 1317–1324. [CrossRef]
28. Bogdan, F.; Tomasz, P.; Krzysztof, Z. Electronic system and signal processing in torque-meter interface of switched reluctance motor drive laboratory test bench. *Prz. Elektrotech.* **2024**, *100*, 59–66. [CrossRef]
29. Lebedev, E.F.; Ostashev, V.E.; Ulyanov, A.V.; Fedorov, V.M.; Shurupov, M.A. Synchronized Active Antenna Arrays for Studying the Passage of Ultra-Wideband Signals in the Atmosphere and Ionosphere. *Dokl. Phys.* **2024**, *68*, 155–158. [CrossRef]
30. Song, X.N.; Chen, Y.; Feng, Z.H.; Hu, G.; Yu, D.-J.; Wu, X.-J. SP-GAN: Self-growing and pruning generative adversarial networks. *IEEE Trans. Neural Netw. Learn. Syst.* **2021**, *32*, 2458–2469. [CrossRef] [PubMed]
31. An, J.W.; Zhuang, C.J.; Rachidi, F.; Zeng, R. An effective EMTR-based high-impedance fault location method for transmission lines. *IEEE Trans. Electromagn. Compat.* **2021**, *63*, 268–276. [CrossRef]

32. Mi, Y.; Guo, J.H.; Wei, W.; Cai, P.C.; Su, X.J.; Fu, Y. Adaptive Allocation Strategy for Power Storage in Isolated DC Microgrid with Unmatched Line Impedance and Abnormal Communication. *CSEE J. Power Energy Syst.* **2025**, *11*, 2241–2250. [CrossRef]
33. Zhao, C.W.; Pian, R.J.; Du, T.S.; Ge, L.J. Rend prediction and analysis model for power quality of important users based on LSTM. *Proc. CSU-EPSA* **2022**, *34*, 26–33. [CrossRef]
34. Ma, X.; Xu, R.L.; Kang, W.F.; Wei, C.Z.; Luo, Y.Y.; Chen, M.Y. Voltage regulation and battery energy storage SoC balancing method for low voltage distribution network with distributed PV and BESS. *J. Chongqing Univ. (Nat. Sci. Ed.)* **2022**, *45*, 9–20. [CrossRef]
35. Zhu, M.; Li, W.X.; Liang, X.D.; Xu, S.; Zhou, B.; Shen, Y. Stepwise voltage drop and transient current control strategies to enhance fault ride-through capability of MMC-HVDC connected DFIG wind farms. *IEEE Trans. Power Syst. A Publ. Power Eng. Soc.* **2021**, *36*, 2127–2137. [CrossRef]
36. Pires Corrêa, H.; Vieira, F.H.T.; de Almeida, M.L.S. An upper bound on magnitude error of voltage drop phasors in distribution lines due to phase transposition assumption. *Electr. Power Compon. Syst.* **2021**, *48*, 1969–1977. [CrossRef]
37. Cai, J.J.; Martorella, M.; Chang, S.Q.; Liu, Q.; Ding, Z.; Long, T. Efficient nonparametric ISAR autofocus algorithm based on contrast maximization and newton's Method. *IEEE Sens. J.* **2021**, *21*, 4474–4487. [CrossRef]
38. Cao, X.Y.; Liu, K.J.R. Distributed newton's method for network cost minimization. *IEEE Trans. Autom. Control* **2021**, *66*, 1278–1285. [CrossRef]
39. Yin, S.L.; Wang, L.G.; Wang, Q.M.; Yang, J.; Jiang, M. Remote Sensing Image Segmentation Based on a Novel Gaussian Mixture Model and SURF Algorithm. *Int. J. Swarm Intell. Res.* **2023**, *14*, 1416–1430. [CrossRef]
40. Tang, W.; Li, T.R.; Zhang, L.; Cai, Y.; Zhang, B.; Wang, Z. Coordinated control of photovoltaic and energy storage system in low-voltage distribution networks based on three-phase four-wire optimal power flow. *Autom. Electr. Power Syst.* **2020**, *44*, 31–40. [CrossRef]
41. Hu, D.H.; Guo, L.; Liu, Y.X.; Zhang, Y.; Li, X.; Liu, H. Stochastic/Robust hybrid optimal dispatching of distribution networks considering fast charging stations with photovoltaic and energy storage. *Power Syst. Technol.* **2021**, *45*, 507–517. [CrossRef]
42. Liu, W.X.; Li, H.S.; Zhou, Y.H.; Yang, M.Y. Coordinated configuration method of cyber and physical equipment in distribution networks based on interval robust control. *Proc. CSEE* **2022**, *42*, 631–639. [CrossRef]
43. Yang, T.; He, Z.Z.; Zhao, D.Y.; Pen, H.B.; Jiang, H.; Cai, S.T.; Yuan, Y.D.; Cai, Y.P. Power quality data loss repair algorithm based on FSOM neural network. *Power Syst. Technol.* **2020**, *44*, 1941–1949. [CrossRef]
44. Adel, H.A.; Amir, S.; Maria, V. A Linear AC Power Flow Model for Unbalanced Multi-Phase Distribution Networks Based on Current Injection Equations. *IEEE Trans. Power Syst. A Publ. Power Eng. Soc.* **2021**, *36*, 3806–3809. [CrossRef]
45. Zhao, B.; Qiu, H.F.; Qin, R.W.; Zhang, X.; Gu, W.; Wang, C. Robust Optimal Dispatch of AC/DC Hybrid Microgrids Considering Generation and Load Uncertainties and Energy Storage Loss. *IEEE Trans. Power Syst. A Publ. Power Eng. Soc.* **2018**, *33*, 5945–5957. [CrossRef]
46. Prasanta, K.J.; Subhojit, G.; Ebha, K. A Binary-Optimization-Based Coordinated Cyber-Physical Attack for Disrupting Electricity Market Operation. *IEEE Syst. J.* **2021**, *15*, 2619–2629. [CrossRef]
47. Saeed, M.R.; Mohsen, H.; Hamidreza, N. Distributed Cooperative Reactive Power Control of PV Systems with Dynamic Leader. *IEEE Trans. Ind. Inform.* **2024**, *20*, 8972–8982. [CrossRef]

Disclaimer/Publisher's Note: The statements, opinions and data contained in all publications are solely those of the individual author(s) and contributor(s) and not of MDPI and/or the editor(s). MDPI and/or the editor(s) disclaim responsibility for any injury to people or property resulting from any ideas, methods, instructions or products referred to in the content.